Electrospectrometry of the Mouse Brain

Xingyun Wang[2, 3, 4], Jean-Claude Béïque[2, 3, 4], and Richard Naud[1, 2, 3, 4 *]

[1]Department of Cellular and Molecular Medicine, University of Ottawa
[2]Department of Physics, University of Ottawa
[3]Center for Neural Dynamics and Artificial Intelligence, University of Ottawa
[4]University of Ottawa Brain and Mind Research Institute University of Ottawa
[*]Corresponding author: rnaud@uottawa.ca

October 1, 2025

Abstract

To understand how electric field fluctuations organize within the brain, we developed deep electrospectroscopy, a method to assess possibly nonlinear spectral similarity between the local field potential of different areas. Applying this technique on recordings from nearly 500 areas of the mouse brain, we reveal an organization made of isolated landmarks and groups of spectrally similar areas. Such communities were mostly found in the forebrain and showed an organization that did not strictly follow the cytoarchitecture. For instance, visual parts of the cortex, colliculus and hippocampal regions were found in the same community. Electrospectral communities were also found to reshape with context, growing in size around brain areas required for a task. These analyses paint a detailed picture of the modularity underlying the structure and dynamics of electroencephalograms.

Introduction

Fluctuations in electric fields recorded on the cranium (electroencephalograms; EEGs) are widely used to help diagnose various neurological conditions [1, 2, 3, 4, 5]. These EEG-based biomarkers rely on spatio-temporal features using methods of spectral decomposition. In many disciplines other than neuroscience, spectral matching reveals fundamental characteristics of a sample's composition. For instance, mass spectrometry relies on the comparison between an observed mass spectrum and a template library to identify a compound. In neuroscience, however, spectral techniques are focusing less on the spectral patterns and more on the specific predominance of a specific fluctuation timescale, an approach that is justified by the rather few and broad spectral peaks in EEG recordings. While this coarse feature-engineering approach has revealed region and task specificity of EEG spectra [6, 7, 8, 9], both the spatial precision and the amplitude of task-induced changes remain low. To resolve this, large datasets of EEG or intracranial EEG (iEEG) have been assembled, introducing the concept of an atlas of these phenomena [10, 11, 12]. Other attempts have dug deeper into the brain, recording local field potentials (LFPs) that recapitulate [13, 14, 15, 16, 17, 18, 19, 20] and extend [21, 22] the features found in the EEG. Integrating large datasets of the LFP revealed increasingly subtle features [23, 24]. These advances suggest that a precise structure of the EEG-LFP may be gained by focusing on a very large, brain-wide dataset, especially when using automated nonlinear spectral matching rather than predefined spectral features.

Results

We developed a three-step approach based on matching possibly non-linear combinations of features of the LFP across brain areas. First, we trained deep artificial neural networks to determine the source area of a spectral sample. Then, the confusion matrix of the trained networks is used to assess the similarity between LFPs from different areas. Third, this metric of similarity is used to delineate an atlas by finding groups of brain areas that appear the same when viewed through LFP spectra.

Such an approach requires large amounts of data. Here we used publicly available, multi-lab, brain wide Neuropixels recordings (International Brain Lab; IBL [25, 26]). In this standardized dataset, mice were cued with an auditory tone and a visual grating to steer a wheel. After quality control and shaping the data for our purposes (see Methods), this data provided LFPs from 472 different brain regions across 127 animals and 12 labs, for a total of 1 687 471 samples taken during the intertrial period. While we present our analysis of this inter-trial period first, we will later present an analysis of another 1.7 M samples taken during the task period.

Nonlinear features of the LFP enable milimetric localization

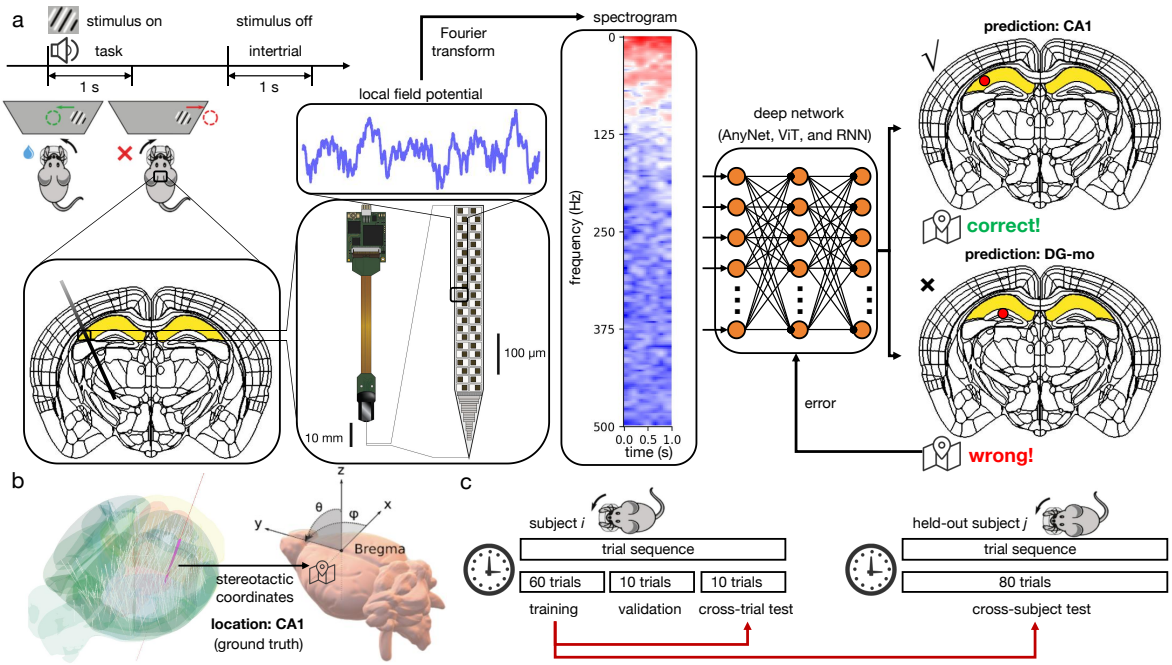

Figure 1: **Deep learning LFP localization a.** Workflow schematic for brain area classification. Opensource Neuropixels data from the IBL was used for both task and intertrial states of a period of 1 second. We used LFP recorded during the inter-trial period. Each LFP on each electrode in each session was converted to a spectrogram and fed to an ANN (ViT, AnyNet or RNN) for localization. The ANN parameters were learned based on correct and erroneous prediction of the brain area of the recording, as illustrated here with a recording localized in cornu ammonis 1 (area 'CA1') but that could have been predicted to lie in the dentate gyrus ('DG-mo'). **b.** The ground truth of a recording's location were obtained by mapping its stereotaxis coordinates to a histologically-defined brain atlas (Allen Brain or Cosmos). **c.** Schematic of training and different test sets. For the first experiment of each subject except held-out subjects, we used first 60 trials to train and the following 10 trials for validation. The last 10 trials from each subject were were used to quantify the cross-trial test. The first 80 trials of held-out subjects consisted of the cross-subject test. Cross-trial and cross-subject tests correspond to in-distribution and out-distribution tests in machine learning.

For each trial and for each channel, we extracted the spectrogram from one second of LFP recordings taken during the inter-trial time period and at the onset of the task (Fig. 1a). The use of LFP spectrograms, or electrospectra, preserved information about interactions between timescales, such as theta-gamma nesting [27, 28], and some information from nearby multi-unit activity and amplitude-phase coupling [29]. To ensure reproducibility, we considered three different classifiers: a deep network developed for sound classification (AnyNet; [30]), a visual transformer (ViT; [31, 32]) and a recurrent neural network (RNN; [33]; Suppl. Fig. 1). We used these neural networks either for regression of the electrode's stereotactic coordinates or for classification of the brain area [34] (Fig. 1a). Data was separated into a training set, a validation set and two test sets. One test set was made of different trials from the same animals used for training, and the other test set was composed of different animals

(Fig. 1c), allowing us to test different types of generalization. Two sets of networks have been trained, one for each time period (task vs inter-trial).

As a preliminary investigation, we inquired about the spatial scale of changes in the electrospectra. Using the inter-trial models for regression (Supplementary Fig. 2) we found positional error between 5 and 9 % of brain length, depending on axis (standard deviation of regression residuals 0.7-1.2 mm, compared to brain length of 14 mm). In comparison, a previous study has estimated the autocorrelation length (equivalent to the positional error of a linear model) of LFPs to a tenth or a third of brain length [35], depending on brain state. This preliminary test supports the idea that our deep networks reveal a more precise structure than the linear methods.

Turning to the classification task, we computed the average cross-trial accuracy for the three neural networks, along with a linear classifier. While a linear classifier was able to localize electrodes far better than chance (accuracy of 0.120 vs 0.002 for chance), its accuracy was surpassed by each of the three deep learning networks (Fig. 2a). Among these, performances were of the same order, with a small advantage for the ViT (0.389) and a small disadvantage for the RNN (0.312) and AnyNet midway (0.368). Therefore, deep learning captures combinations of features in the electrospectra that were not captured with linear methods.

To gain insights on the type of features exploited by the models, we also trained our models to classify time-averaged spectra instead of time-resolved spectrograms (Suppl. Fig. 3). In this case, the linear classifier upkept its accuracy (0.119), but the accuracy of the deep models dropped (AnyNet 0.213, ViT 0.357, RNN 0.176). This indicates that information increases from linear features to nonlinear feature combinations of the time-averaged spectra, and increases further with nonlinear feature combinations of spectrograms.

Deep learning reveals multiple electrospectral landmarks

We then asked what makes one area more recognizable than another. Plotting the accuracy area-by-area (Fig. 2b,c), we found a considerable variability. We performed a multivariate regression of the region-specific accuracy on four factors: i) the volume of the brain area, ii) the number of samples (Fig. 2d), iii) the recording depth, which could decrease the accuracy via an increased stereotactic error but could also indicate more recognizable deeper structures either intrinsically or by bearing less artifacts of the surgery, and iv) the number of subjects. We found that the main factors affecting the cross-trial accuracy are the volume and the sample number, while the depth and subject numbers have comparatively negligible contributions (Fig. 2d). Surprisingly, depth was positively associated with accuracy, suggesting a small stereotaxis error and more recognizable deeper regions. These factors, however, could not account for the majority of the variability (regression R^2=0.14). Therefore, the considerable variability in localization accuracy is not fully accountable by size and number of samples and supports the idea that some areas are intrinsically more recognizable than others.

We call those more recognizable areas 'landmarks'. Examples from the cross-trial test are the main olfactory bulb (MOB), cornus ammonis 1 (CA1) and the different layers of the dentate gyrus (DG; Fig. 2b,c). Turning to the cross-subject test, here we expect that variability in brain morphologies will necessarily reduce the maximal accuracy. Also, since most areas were not sampled consistently across animals, we could only perform this cross-subject test for a fraction of the areas (see Methods). Cross-subject accuracies for the remaining areas are shown in Figure 2e. A number of cross-subject landmarks can be identified by virtue of their relatively high accuracy. These include CA1, CA3 and each of the three layers of DG. We also found landmarks outside these areas known for their distinctive LFP: the lateral posterior nucleus (LP) and the posterior complex (PO) of the thalamus, hindbrain's medial vestibular nucleus (MV) and the cerebellum's Lobule IV (CUL4 5). Given the added difficulty of the cross-subject test, it remains possible that these accuracies mainly reflect the number of subjects. To verify this, we selected two areas, non-landmark VISa5 (visual cortex, anterior area, layer 5) and landmark DG-mo (dentate gyrus, molecular layer), and gradually increased the subject number in the training set while testing in held-out subjects (Fig. 2f). As expected, the accuracy gradually increased with the number of animals in the training set. Yet, VISa5 required 35 subjects to match the accuracy achieved by DG-mo with only 5 subjects, further supporting that DG-mo is a landmark of the LFP. To more broadly test whether a landmark identified in cross-trial tests is predictive of landmark status in cross-subject tests, we calculated the correlation between cross-trial and cross-subject accuracies (Fig. 2g). We found a positive correlation, thus supporting the idea that we can identify subject invariant electrospectral landmarks from cross-trial tests.

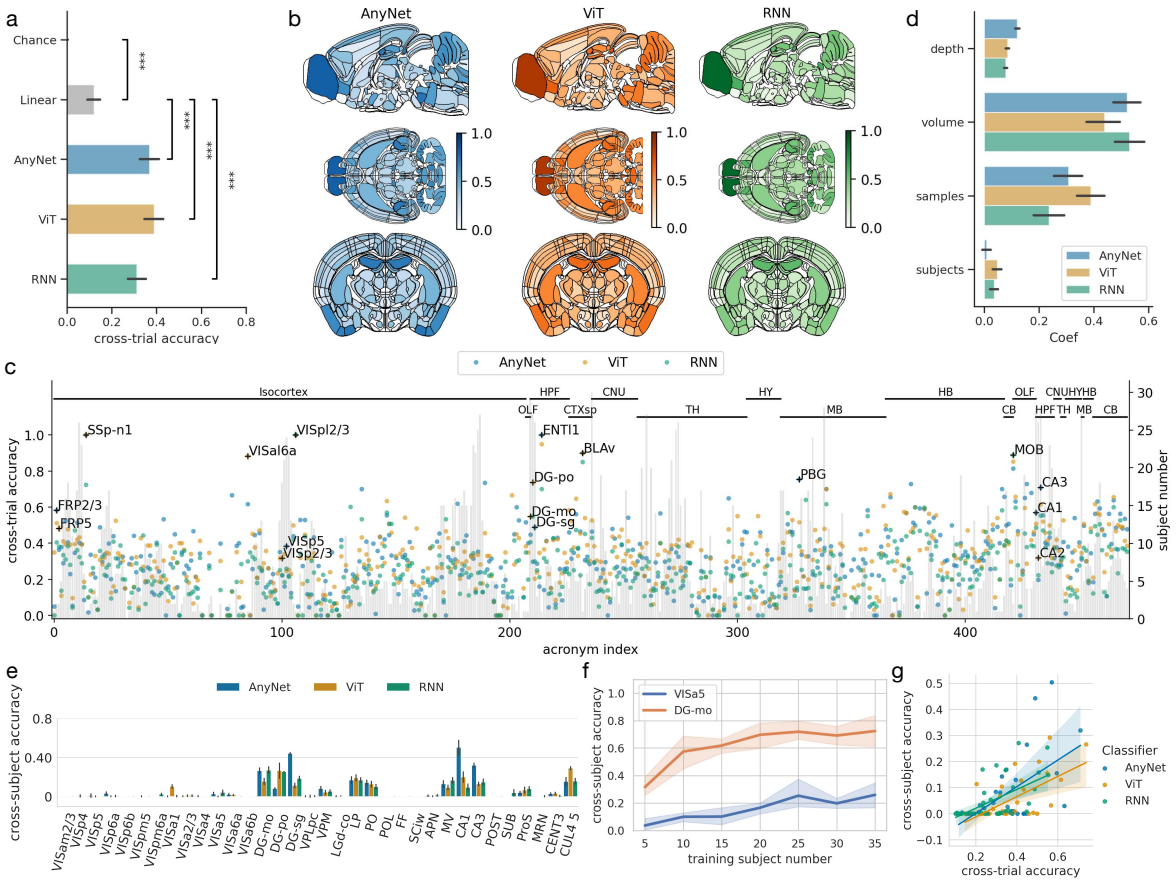

Figure 2: **Electrospectral landmarks show high accuracy across trials and subjects a.** Overall cross-trial accuracy from distinct classifiers: linear network model, AnyNet, ViT, and RNN. Linear classifier performs significantly better than the chance level ($p < 0.001$). The three deep networks (AnyNet, ViT, and RNN) outperform the linear classifier ($p < 0.001$). **b.** Beta coefficients of multi-linear regression of cross-trial accuracy against depth, volume, samples and number of subjects. **c.** Spatial distribution of individual cross-trial accuracy from three classifiers across the mouse brain. **d.** Individual cross-trial accuracy (left axis) of the three deep learning models for the 472 brain regions. At the top of the figure is the label of the anatomical divisions. The subject number of each brain region is shown as gray bars referring to the right-axis. **e.** Cross-subject accuracy for brain areas having at least have 10 subjects. **f.** AnyNet cross-subject accurcay while holding out 5 subjects and gradually increasing the subject number in the training dataset. **g.** Scatter plot of cross-subject against cross-trial accuracies. Pearson Correlation between cross-trial accuracy and cross-subject accuracy are AnyNet $r = 0.587$, $p = 0.00027$; ViT $r = 0.334$, $p = 0.0537$; RNN $r = 0.501$, $p = 0.00252$. See Supplementary Table 1 for acronym definition.

Electrospectral localization transfers to human

We further investigated the idea that our models trained on mice can then be fine-tuned on limited data to localize LFP from human brains, indicating a shared electrospectral structure across species. To investigate this, we used a human Neuropixels dataset, which was recorded from the dlPFC and temporal lobe [36]. We refined the recording location based on distinct channels to get 21 brain region labels and used our three classifiers as we did for mice. We compared two training approaches: i) training classifiers from randomly initialized weights on the human dataset and ii) training classifiers that were pre-trained on the large mice dataset while only allowing the penultimate layer weights to be changed. If there is a shared structure across species, we should observe a faster learning in the pre-trained group. The final accuracy, in contrast, is more likely to reflect the restriction of which weight is allowed to be trained. We found that classifiers pre-trained with mice data could learn much faster than their counterparts trained from a random initialization on the human dataset (Suppl. Fig.

4). The final cross-trial accuracy did not show a significant difference between the transfer learning and random initialization group. This result further supports the potential for generalization of the electrospectral features learned by the models.

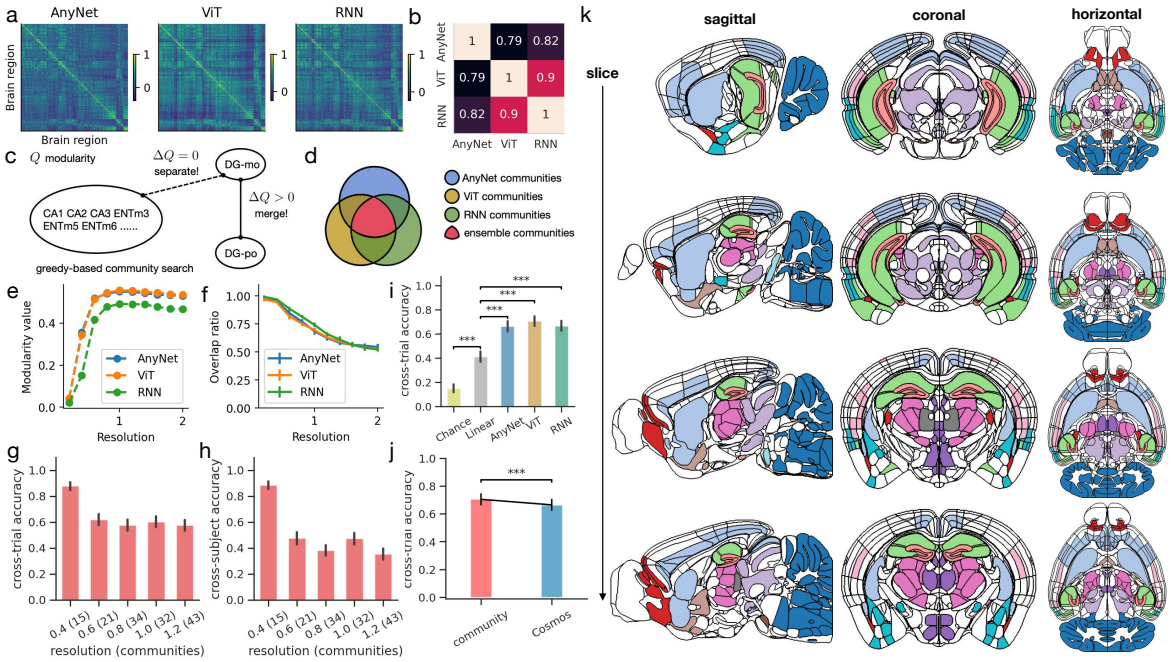

Figure 3: **Spectral similarities define communities a**. Heat map showing the representational correlation matrices across 472 brain regions, each pixel depicts the correlation coefficient of the classifier's penultimate layer activations of one Allen brain atlas area to another. **b**. Similarity analysis for the correlation matrices of the three different models, each square shows the correlation coefficient between the matrices shown in a. **c**. Schematics of greedy modularity search for communities in 472 brain regions. If merging two separated communities increases overall modularity, then a new community is generated; otherwise, those two communities remain isolated modules. **d**. Schematic for establishing a consensus across ANNs. Ensemble communities are obtained by first aligning each community across ANNs and then only keeping the brain areas that were found to belong to that community consistently across the three ANNs. **e**. Final modularity values of greedy search is shown for different resolutions. **f.** The overlap ratio between communities found using all brain areas and communities found using 80 % of the brain areas. **g**. Cross-trial accuracy for ensemble communities at different resolutions, the number of communities in parentheses. **h**. Same as g but for cross-trial accuracy. **i**. Overall cross-trial accuracy for the different algorithms trained to classify the 10-region anatomical atlas 'Cosmos'. **j**. Comparing community with Cosmos at a matched number of 10 classes. The cross-trial classification accuracy is shown for the top-10, landmark, communities and compared with the 10-region anatomical atlas, Cosmos. **k**. Sagittal, coronal and horizontal slices showing 18 ensemble communities out of the 32 using different colors. Only 18 are shown for enhanced visualization, hence the white areas are either areas that did not belong to any community, or areas that were in the 14 communities that could not be shown simultaneously.

Electrospectral similarities reveal robust communities

Inspired by spectroscopy approaches that rely on spectral matching to identify the composition of a sample, we hypothesized that a group of areas may share electrospectral features even if LFP spectra do not show well-separated peaks. Because the relevant spectral features may not be combined linearly (Fig. 2a), we rely on the ANN representations of electrospectra rather than the electrospectra themselves. Such inter-area similarity is illustrated with the correlation matrix of the representation at the penultimate layer (Fig. 3a), which shows a structure conserved across ANNs (Fig. 3b). We thus applied an approach from graph theory to delineate shared spectral features. The generalized

modularity index [37] uses the ANN's confusion matrices to create an undirected weighted graph and then quantifies the degree to which a given community structure is unlikely to arise from a random graph. The index is defined with a hyperparameter called the resolution (see Methods), which favors big communities when it is small, or small communities when it is large. Given a resolution parameter, a greedy modularity search [38] proceeds by sequentially grouping or splitting communities to find the structure that maximizes modularity (Fig. 3c). Furthermore, to ensure that we find a community structure that does not depend on the specific deep network architecture, we performed the modularity search on each network independently and then focused on areas that are at the intersection between the communities found using each classifier (Fig. 3d).

Before analyzing this electrospectral atlas, we first had to evaluate its reliability. Figure 3e shows the optimal modularity as a function of resolution. As a rule-of-thumb for modularity-based approaches, the index should be higher than 0.3 [39, 40], which is achieved for resolutions higher than 0.5. The modularity index showed a clear optimum, such that it was maximized by a resolution near unity. As higher resolutions yield smaller communities, we checked the robustness of the communities at different resolutions by bootstrapping (Fig. 3f) and found a monotonically decreasing robustness with an overlap ratio at 75% when using a resolution of 1. We also computed the cross-trial and cross-subject accuracies for the classifications of communities found at different resolutions (Fig. 3g-h). Here the resolution showed only a small effect on robustness, and only the non-modular resolution (0.4) was markedly more robust, an observation explained by the very large communities that bias the accuracy due to class imbalance (Suppl. Fig. 5a). The cross-trial accuracy fluctuated around 0.6 while the cross-subject accuracy around 0.4, matching the accuracies of individual landmark areas (Fig. 2). Together, this technique allows us to find a reliable community structure in the LFP, which, along with isolated landmarks, contributes to the electrospectral atlas of the mouse brain.

Next we sought to compare the localization accuracies of an atlas based on the electrospectral communities and one based on a coarse histological atlas. We thus trained our classifiers on an atlas of ten mouse brain regions (e.g. olfactory bulb, isocortex, see Fig. 4b). Referring to this map as the Cosmos Atlas [25], we found again that a linear classifier was more apt than chance but surpassed by deep networks (Fig. 3i, Suppl. Fig. 6). The deep networks achieved a cross-trial accuracy around 0.65. We could then directly compare the Cosmos Atlas with the 10 most recognizable communities, thus matching the task difficulty. Even at a resolution of one, which separates the brain into much smaller regions than Cosmos and does not contain landmark areas, it is easier to localize communities of the electrospectral atlas (Fig. 3j).

Electrospectral communities of the intertrial period

Focusing on a selected set of communities, Figure 4 shows the resulting network graph with communities denoted by different colors (see also exemplar spectrograms in Suppl. Fig. 7 and full list in Suppl. Table 1). We stress that the links in the graph denote spectral similarity, not synaptic connections between areas. Many communities suggested an alignment with function. For instance, we found an 'audio-visual community' composed of the union of auditory cortex, parts of higher-order visual cortex, temporal and parietal association areas, a 'hippocampus community' which regrouped CA1, CA2, CA3 with entorhinal cortex, the 'olfactory community' regrouped parts of the olfactory bulb with frontal pole and orbitofrontal cortex, or a 'visuo-vibrissal community' that unites lateral and anterior visual cortex with temporal association areas and barrel fields. The alignment with function was also suggested by subcortical communities such as a 'auditory reflexes community', which united superior olive (SOCI), inferior colliculus (ICc), a nucleus for the acoustic startle response (PRNc), and one for the tensor tympanic muscle (PC5). The 'amygdala community' regrouped the lateral amygdalar nucleus (LA) with the piriform amygdalar area of the olfactory bulb (PAA) and the cortical amygdalar area (COA). Alignment with function was not manifest for all communities, such as the large 'cerebellum-hindbrain' community, or the union of three small and deep areas we called 'raphe' (Fig. 4a).

Broadly, however, this organization was correlated but not strictly aligned with the broad cytoarchitectural regions of the brain (Fig. 4b). For example, the putamen and secondary motor cortex were central hubs (see examples of hubs in Suppl. Fig. 8) of a community that unites nucleus accumbens, gustatory cortex, parts of the somatosensory, anterior cingulate and insular cortex. Because many of these areas are part of the cortico-basal-ganglia loop, receiving inputs from the parafascicular nucleus, we labeled this community 'motor-premotor'. Similarly, at the center of the 'core visual community', which contains the optic parts of colliculus, primary visual cortex, parts of retrosplenial cortex and

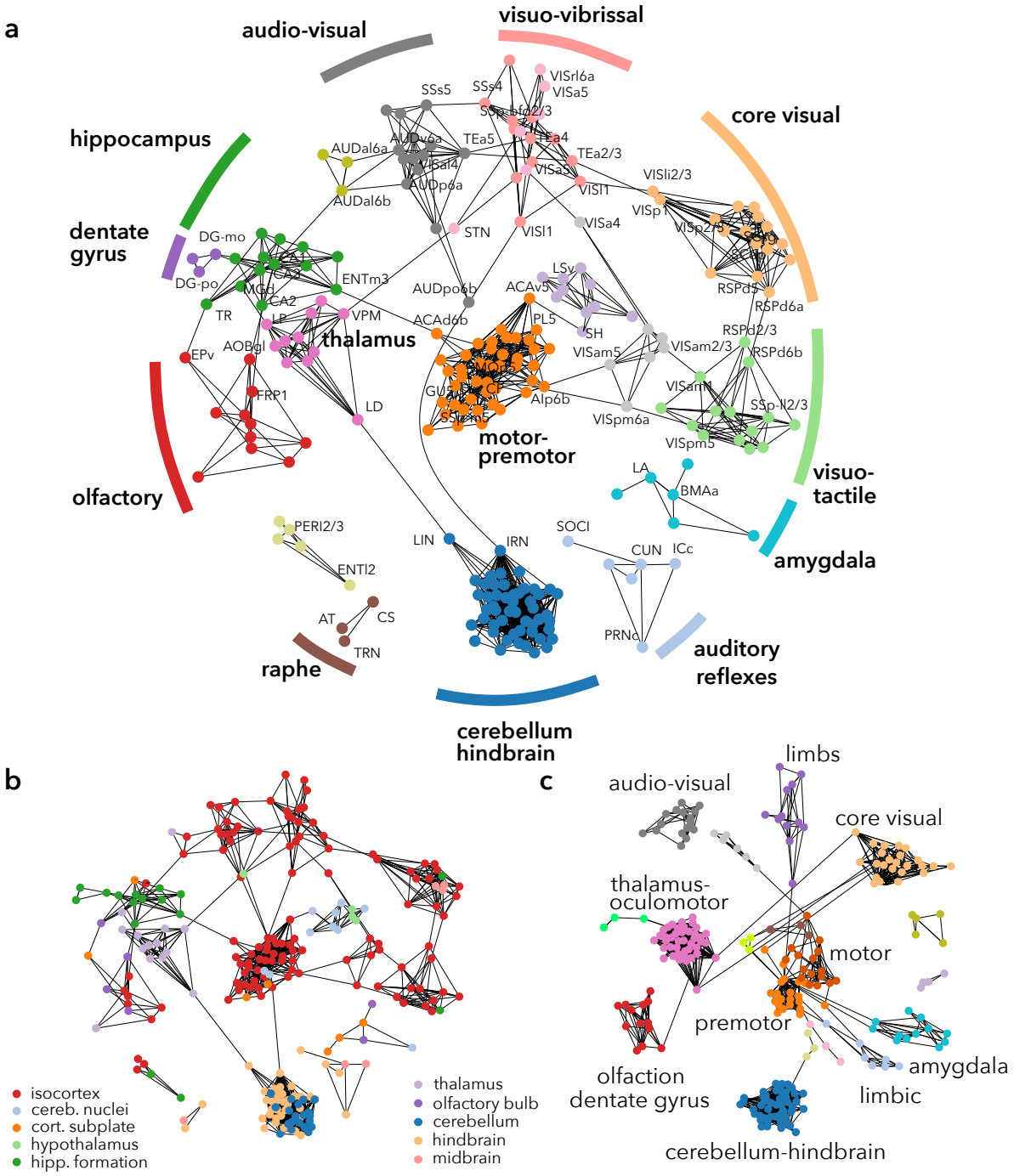

Figure 4: **Electrospectral communities of the inter-trial and task onset contexts.** **a** A subset of electrospectral communities identified during the inter-trial state at resolution 1. Each circle represent an Allen atlas area, a subset is labeled with their acronyms. Circle color refers to community, with a subset labeled based on area composition. Graph links represent thresholded elements of the confusion matrix, with thicker lines corresponding to higher values of the confusion matrix. **b** same graph as panel a but colors representing coarse histological atlas. **c** Electrospectral communities found during the audio-visual cue period. The colors were chosen to align with panel a but some communities had no clear equivalence. A table for all communities and a focus on different subsystems are presented in supplementary materials.

area prostriata, but not many other associative parts of the visual cortex. The motor parts of the superior colliculus were instead separated into two communities (Suppl. Fig. 10), one containing many hypothalamic areas, and one containing oculomotor parts of the midbrain. Therefore, we find that electrospectral communities deviate from the cytoarchitecture in a way that suggests an alignment with function.

Electrospectral communities reshape according to the task

To establish the community structure in a different context, we used the other set of models trained on the 1.7 M LFP samples of the task period. The IBL task required visual and auditory acuity, a mapping from a visual grating to a motion, lower and upper limb coordination for turning a wheel and licking for obtaining rewards. The communities were established anew using the same resolution parameter (Fig. 4c, exemplar spectrograms in Suppl. Fig. 9, and subsystems task-intertrial comparisons in Suppl. Fig. 10 -Fig. 13). We found that some communities appeared (a union of lower and upper limbs), some disappeared (visuo-vibrissal, visuo-tactile), some communities stayed approximately the same (visuo-auditory, visual-am, septum, amygdala) and many reshaped by adding or removing areas for a set of core areas.

Consistent with the appearance of the drifting grating, vision-related communities showed much reshaping. The core visual community increased in size (17 areas in the intertrial period vs. 25 in task), with the inclusion of visual areas VISpm and VISa). The visual parts of the colliculus and area prostriata remained in this community, which also remained centered on layer 5 of the primary visual cortex (VISp5). Plotting the network graph of all communities containing subcortical visual and auditory areas (Suppl. Fig. 10), we observed that SCsg (a visual layer of superior colliculus) preserved some similarity with SCiw (intermediate white layer). SCiw belongs to a large community that contains motor and association parts of the superior colliculus along with oculomotor hindbrain and a large portion of thalamus, a merger of the oculomotor and thalamus communities of the intertrial period. Interestingly, a new small community appeared that contained both the visual and auditory relay thalamus despite these areas being dominated by categorically different afferents. These relay areas did not belong to any community in the intertrial period. Together, the picture that arises is that audio-visual areas scattered in many communities during the intertrial period, and lumped together in larger communities during the task.

Motor and planning areas were marked by a split. The large community which, during the intertrial period, centered on putamen became separated, such that putamen (CP) connected with the frontal areas (frontal pole (FRP) and anterior cingulate area (ACA)) and part of the secondary motor cortex (MOs). Putamen became most similar with the community that integrated somatosensation of the upper and lower limbs. Splitting from the large motor community of the intertrial period was a community that contained somatosensory mouth (SSp-m) and nose (SSp-n), the claustrum (CLA) as well as primary motor (MOp), agranular and insular cortex (AI). This split potentially reflects the two components motor components associated with this period, a task-specific motor plan related to limbs and a reward-related licking. Some links from these motor-premotor communities narrowed down to a single pair of areas showing electrospectral resemblance (Suppl. 14). During the task onset, these links are between putamen and upper limb layer 6b from the combined limbs community, and between mouth somatosensory layer 6a and 5 from the gustatory community.

Conclusion

Overall, we have shown that the LFP preserves similarities across contiguous and non-contiguous regions of the brain, forming functional and dynamic modules that reshape according to the context. This implies that task-dependent changes observed in the EEG are underpinned by such reshaping of LFP modules.

References

[1] Susan T Herman, Nicholas S Abend, Thomas P Bleck, Kevin E Chapman, Frank W Drislane, Ronald G Emerson, Elizabeth E Gerard, Cecil D Hahn, Aatif M Husain, Peter W Kaplan, et al.

Consensus statement on continuous eeg in critically ill adults and children, part i: indications. *Journal of Clinical Neurophysiology*, 32(2):87–95, 2015.

[2] Shelagh JM Smith. Eeg in the diagnosis, classification, and management of patients with epilepsy. *Journal of Neurology, Neurosurgery & Psychiatry*, 76(suppl 2):ii2–ii7, 2005.

[3] Gráinne McLoughlin, Scott Makeig, and Ming T Tsuang. In search of biomarkers in psychiatry: Eeg-based measures of brain function. *American Journal of Medical Genetics Part B: Neuropsychiatric Genetics*, 165(2):111–121, 2014.

[4] Victor J Geraedts, Lennard I Boon, Johan Marinus, Alida A Gouw, Jacobus J van Hilten, Cornelis J Stam, Martijn R Tannemaat, and Maria Fiorella Contarino. Clinical correlates of quantitative eeg in parkinson disease: A systematic review. *Neurology*, 91(19):871–883, 2018.

[5] Christoph Lehmann, Thomas Koenig, Vesna Jelic, Leslie Prichep, Roy E John, Lars-Olof Wahlund, Yadolah Dodge, and Thomas Dierks. Application and comparison of classification algorithms for recognition of alzheimer's disease in electrical brain activity (eeg). *Journal of neuroscience methods*, 161(2):342–350, 2007.

[6] Alexander Craik, Yongtian He, and Jose L Contreras-Vidal. Deep learning for electroencephalogram (eeg) classification tasks: a review. *Journal of neural engineering*, 16(3):031001, 2019.

[7] Christoph Mulert, Lorenz Jäger, Robert Schmitt, Patrick Bussfeld, Oliver Pogarell, Hans-Jürgen Möller, Georg Juckel, and Ulrich Hegerl. Integration of fmri and simultaneous eeg: towards a comprehensive understanding of localization and time-course of brain activity in target detection. *Neuroimage*, 22(1):83–94, 2004.

[8] Alan Gevins, Michael E Smith, Linda McEvoy, and Daphne Yu. High-resolution eeg mapping of cortical activation related to working memory: effects of task difficulty, type of processing, and practice. *Cerebral cortex (New York, NY: 1991)*, 7(4):374–385, 1997.

[9] Arne Dietrich and Riam Kanso. A review of eeg, erp, and neuroimaging studies of creativity and insight. *Psychological bulletin*, 136(5):822, 2010.

[10] Birgit Frauscher, Nicolas Von Ellenrieder, Rina Zelmann, Irena Doležalová, Lorella Minotti, André Olivier, Jeffery Hall, Dominique Hoffmann, Dang Khoa Nguyen, Philippe Kahane, et al. Atlas of the normal intracranial electroencephalogram: neurophysiological awake activity in different cortical areas. *Brain*, 141(4):1130–1144, 2018.

[11] Karim Jerbi, Tomás Ossandón, Carlos M Hamamé, S Senova, Sarang S Dalal, Julien Jung, Lorella Minotti, Olivier Bertrand, Alain Berthoz, Philippe Kahane, et al. Task-related gamma-band dynamics from an intracerebral perspective: Review and implications for surface eeg and meg. *Human brain mapping*, 30(6):1758–1771, 2009.

[12] Wenhui Cui, Woojae Jeong, Philipp Thölke, Takfarinas Medani, Karim Jerbi, Anand A Joshi, and Richard M Leahy. Neuro-gpt: Towards a foundation model for eeg. In *2024 IEEE International Symposium on Biomedical Imaging (ISBI)*, pages 1–5. IEEE, 2024.

[13] Wolfgang Klimesch. Alpha-band oscillations, attention, and controlled access to stored information. *Trends in cognitive sciences*, 16(12):606–617, 2012.

[14] Charline Peylo, Yannik Hilla, and Paul Sauseng. Cause or consequence? alpha oscillations in visuospatial attention. *Trends in Neurosciences*, 44(9):705–713, 2021.

[15] Rosanne M Van Diepen, John J Foxe, and Ali Mazaheri. The functional role of alpha-band activity in attentional processing: the current zeitgeist and future outlook. *Current opinion in psychology*, 29:229–238, 2019.

[16] György Buzsáki and Xiao-Jing Wang. Mechanisms of gamma oscillations. *Annual review of neuroscience*, 35:203–225, 2012.

[17] Supratim Ray and John HR Maunsell. Do gamma oscillations play a role in cerebral cortex? *Trends in cognitive sciences*, 19(2):78–85, 2015.

[18] Ole Jensen, Jochen Kaiser, and Jean-Philippe Lachaux. Human gamma-frequency oscillations associated with attention and memory. *Trends in neurosciences*, 30(7):317–324, 2007.

[19] Ole Jensen, Bart Gips, Til Ole Bergmann, and Mathilde Bonnefond. Temporal coding organized by coupled alpha and gamma oscillations prioritize visual processing. *Trends in neurosciences*, 37(7):357–369, 2014.

[20] Antonio Fernandez-Ruiz, Anton Sirota, Vítor Lopes-dos Santos, and David Dupret. Over and above frequency: gamma oscillations as units of neural circuit operations. *Neuron*, 111(7):936–953, 2023.

[21] György Buzsáki. Hippocampal sharp wave-ripple: A cognitive biomarker for episodic memory and planning. *Hippocampus*, 25(10):1073–1188, 2015.

[22] Bernhard P Staresina and Maria Wimber. A neural chronometry of memory recall. *Trends in cognitive sciences*, 23(12):1071–1085, 2019.

[23] Yuta Senzai and György Buzsáki. Physiological properties and behavioral correlates of hippocampal granule cells and mossy cells. *Neuron*, 93(3):691–704, 2017.

[24] Diego Mendoza-Halliday, Alex James Major, Noah Lee, Maxwell J Lichtenfeld, Brock Carlson, Blake Mitchell, Patrick D Meng, Yihan Xiong, Jacob A Westerberg, Xiaoxuan Jia, et al. A ubiquitous spectrolaminar motif of local field potential power across the primate cortex. *Nature Neuroscience*, 27(3):547–560, 2024.

[25] Larry F Abbott, Dora E Angelaki, Matteo Carandini, Anne K Churchland, Yang Dan, Peter Dayan, Sophie Deneve, Ila Fiete, Surya Ganguli, Kenneth D Harris, et al. An international laboratory for systems and computational neuroscience. *Neuron*, 96(6):1213–1218, 2017.

[26] International Brain Laboratory, Valeria Aguillon-Rodriguez, Dora Angelaki, Hannah Bayer, Niccolò Bonacchi, Matteo Carandini, Fanny Cazettes, Gaelle Chapuis, Anne K Churchland, Yang Dan, et al. Standardized and reproducible measurement of decision-making in mice. *Elife*, 10:e63711, 2021.

[27] Erik W Schomburg, Antonio Fernández-Ruiz, Kenji Mizuseki, Antal Berényi, Costas A Anastassiou, Christof Koch, and György Buzsáki. Theta phase segregation of input-specific gamma patterns in entorhinal-hippocampal networks. *Neuron*, 84(2):470–485, 2014.

[28] John E Lisman and Ole Jensen. The theta-gamma neural code. *Neuron*, 77(6):1002–1016, 2013.

[29] Gemechu Bekele Tolossa, Aidan M Schneider, Eva Dyer, and Keith B Hengen. Neurons throughout the brain embed robust signatures of their anatomical location into spike trains. *eLife*, 13:RP101506, 2025.

[30] Ilija Radosavovic, Raj Prateek Kosaraju, Ross Girshick, Kaiming He, and Piotr Dollár. Designing network design spaces. In *Proceedings of the IEEE/CVF conference on computer vision and pattern recognition*, pages 10428–10436, 2020.

[31] Ashish Vaswani, Noam Shazeer, Niki Parmar, Jakob Uszkoreit, Llion Jones, Aidan N Gomez, Łukasz Kaiser, and Illia Polosukhin. Attention is all you need. *Advances in neural information processing systems*, 30, 2017.

[32] Alexey Dosovitskiy, Lucas Beyer, Alexander Kolesnikov, Dirk Weissenborn, Xiaohua Zhai, Thomas Unterthiner, Mostafa Dehghani, Matthias Minderer, Georg Heigold, Sylvain Gelly, et al. An image is worth 16x16 words: Transformers for image recognition at scale. *arXiv preprint arXiv:2010.11929*, 2020.

[33] Patel Dhruv and Subham Naskar. Image classification using convolutional neural network (cnn) and recurrent neural network (rnn): A review. *Machine learning and information processing: proceedings of ICMLIP 2019*, pages 367–381, 2020.

[34] Susan M Sunkin, Lydia Ng, Chris Lau, Tim Dolbeare, Terri L Gilbert, Carol L Thompson, Michael Hawrylycz, and Chinh Dang. Allen brain atlas: an integrated spatio-temporal portal for exploring the central nervous system. *Nucleic acids research*, 41(D1):D996–D1008, 2012.

[35] Alain Destexhe, Diego Contreras, and Mircea Steriade. Spatiotemporal analysis of local field potentials and unit discharges in cat cerebral cortex during natural wake and sleep states. *Journal of Neuroscience*, 19(11):4595–4608, 1999.

[36] Angelique C Paulk, Yoav Kfir, Arjun R Khanna, Martina L Mustroph, Eric M Trautmann, Dan J Soper, Sergey D Stavisky, Marleen Welkenhuysen, Barundeb Dutta, Krishna V Shenoy, et al. Large-scale neural recordings with single neuron resolution using neuropixels probes in human cortex. *Nature Neuroscience*, 25(2):252–263, 2022.

[37] Mark EJ Newman. Modularity and community structure in networks. *Proceedings of the national academy of sciences*, 103(23):8577–8582, 2006.

[38] Aaron Clauset, Mark EJ Newman, and Cristopher Moore. Finding community structure in very large networks. *Physical Review E—Statistical, Nonlinear, and Soft Matter Physics*, 70(6):066111, 2004.

[39] David Meunier, Renaud Lambiotte, Alex Fornito, Karen Ersche, and Edward T Bullmore. Hierarchical modularity in human brain functional networks. *Frontiers in neuroinformatics*, 3:571, 2009.

[40] David Meunier, Renaud Lambiotte, and Edward T Bullmore. Modular and hierarchically modular organization of brain networks. *Frontiers in neuroscience*, 4:200, 2010.

[41] International Brain Laboratory, Dora Angelaki, Brandon Benson, Julius Benson, Daniel Birman, Niccolò Bonacchi, Kcénia Bougrova, Sebastian A Bruijns, Matteo Carandini, Joana A Catarino, et al. A brain-wide map of neural activity during complex behaviour. *Nature*, 645(8079):177, 2025.

[42] Guido Meijer Huntenburg, Liam Paninski, Michael Schartner, Karel Svoboda, Miles Wells, Matthew R Whiteway, Olivier Winter, et al. Video hardware and software for the international brain laboratory.

[43] Alex Graves, Marcus Liwicki, Santiago Fernández, Roman Bertolami, Horst Bunke, and Jürgen Schmidhuber. A novel connectionist system for unconstrained handwriting recognition. *IEEE transactions on pattern analysis and machine intelligence*, 31(5):855–868, 2008.

Supplementary Materials

Methods

International Brain Lab

We used brain-wide Neuropixels recordings from International Brain Lab (IBL) [41], which was recorded across 139 mice in 12 labs. During the experiment, the mouse did a visual discrimination task requiring it to turn a wheel to move a visual stimulus (an oriented Gabor having variable contrasts) to the center of the screen. The mouse needed to hold the wheel still for 0.4-0.7 s to start a new trial, which was announced by an auditory cue. All mice were first trained and rewarded with sweetened water when they made correct decisions. Wrong decisions would bring a noise burst and longer inter-trial interval (2 s) as a punishment. Before the visual stimulus was turned off, the mouse had enough time for collecting the reward. Additional information for surgical methods, experimental materials, and probe tracking and alignment can be found in [26, 42]. All animal experiments were conducted according to local laws and approved by the institutional ethics committees [41]. Details for mice like housing, weights, and genders can be found in [41]. To collect samples from as many areas as possible brain areas, we used brain areas in Beryl mapping in case some recorded areas couldn't be localized precisely under the Allen brain atlas (e.g., CA1so, CA1sp and CA1sr were labeled as CA1). We didn't distinguish between hemispheres. The time period of interest was 1 second. For the intertrial period it is immediately after the visual stimulus was turned off and for the task period it is immediately after the visual stimulus was turned on. In some rare cases, the inter-trial time interval was smaller than 1 second, such that the inter-trial period contained part of this stimulus period. This only occurred on 0.06% of the trials. In all, we collected 3.4 million LFPs ($\leq$ 500 Hz) samples from 472 brain areas for 1 second in the inter-trial and the task states.

Data preprocessing

Spectrogram

For each 1 second sample of the LFP, acquired at 2500 Hz sampling frequency, we performed a Fast Fourier Transformation (FFT) with 401 bins, window length 800 sample points (320 ms), and hop of window length 400 sample points (160 ms), which results in frequency resolution of 3 Hz. We limited the frequency for analysis between 3 and 500 Hz. This results in a time-resolved spectrum (spectrogram) of dimension 224×28, where the first dimension is the frequency and the second dimension is time. We used the square root of the power so as to better preserve activity in the ripple band and beta band. This frequency range should still bear signatures of the action potentials nearby [**?**] and harmonics of rhythms slower than 3 Hz. The time-resolved spectra should also still keep partial information about rhythm nesting.

Cross validation

For each brain region, we assembled a dataset from multiple subjects. For each subject, we kept only the first 80 trials to help balance data across subjects. As a training set, we used only the first 60 trials and only for a fraction of the animals. The following 10 trials of each subject constituted the validation test. The last 10 trials of the same animals made the cross-trial test set. Some animals were held out to constitute the cross-subject test. To determine which animals were held out and which were used for the training set, we calculated the subject number for samples of each recorded brain area. We only held out subjects that would not make the sampled subject numbers for each recorded area less than 10. The cross-subject test set is then made up of the first 80 trials in the first experiment of each held-out subject.

Human data

We used publicly available Neuropixels recordings in humans, which were acquired from the dlPFC and the temporal lobe [36]. To refine the recording location, for one penetration in one coarse brain region, which had recordings from 384 channels, we only preserved one channel every 60 channels and labeled it as a new brain area index. Finally, we got 21 refined brain regions in all. All preprocessing

from LFPs to the input spectrogram of the human data was the same as mice data. For each fine brain region, we had 2 000 samples, each for 1 second. We used the first 1400 samples for training, the next 200 as validation, and reserved the last 400 for testing. In all, we had 42 000 labeled samples of human LFP.

Neural networks

Classifier architectures

The Recurrent Neural Network (RNN), the Convolutional Neural Network (CNN), and the Transformer are three basic types of modern deep network architectures. The RNN focuses on extracting sequential information with the risk of ignoring global information. The CNN extracts the local features and assembles them into a global representation by the convolution process. The self-attention mechanism in the Transformer enables the algorithm to integrate global sequential information; its quadratic computational complexity makes the training expensive.

For the RNN architecture, we treated the size of the frequency dimension of the input as the input size and the time dimension as the sequential dimension, as shown in Suppl. Fig. 5. We chose a two-layer, gated recurrent unit (GRU) module with 512 hidden units per layer. The last dimension of the output from the GRU module [43], which integrates previous sequence information, is fed into a linear layer that had the same number units as the number of brain regions. The RNN is not bi-directional because of our causal assumption of the spectrogram.

For the CNN architecture, considering the input as an image, we implemented the AnyNet framework to design our model [30]. AnyNet is a semi-auto neural architecture design framework for computer vision tasks, as shown in Suppl. Fig. 5. AnyNet consists of a stem, a body and a head. The stem was used to implement the initial processing for the spectrogram; multiple blocks exist in the body to generate the final representation by sequential nonlinear transformations; the head uses the linear readout to convert the output representation from the body to the brain region category. The architecture parameters include depth d_i, the number of the output channels c_i, the number of groups g_i, and bottleneck ratio k_i for stage i. The AnyNet design principles are the bottleneck ratio $k_i = k$, group width $g_i = g$ for all stages i; increase network width, depth across stages, which $c_i \leq c_{i+1}$, $d_i \leq d_{i+1}$. In this proposal, considering the principles and the limitations of our hardware, we designed our AnyNet as having no bottleneck and the group width is always set to be 1, in which $k_i = 1$ and $g_i = 1$; the channel number c_0 for the stem was 64, and the channel number for the remaining blocks was $c_i = c_0 * (i + 1)$; the depth for all stage was $d_i = 2$.

For the Transformer architecture, we still treated the input as an image and used the Vision Transformer (ViT) model [32], as shown in Suppl. Fig. 5. We separated the input into 8 patches, with each patch size being 28×28. A $< cls >$ token was also fed with 8 patches. After cascade transformation, its representation will be mapped into the output brain region label by a linear layer combined with the Softmax function. We implemented 8 heads and 4 Transformer encoder blocks in our ViT model.

Classifier training

As a typical method, we implemented cross-entropy to measure the loss between the label and model output for all three architectures. We used the Adam algorithm as the optimizer for training our models and set the batch size as 256. To avoid overfitting, the validation set was used for early stopping, in which we only retained models which had the best validation accuracy with training accuracy ≥ 0.6.

Computing resources

Our deep-learning based classifiers were trained by one A100 GPU. For an AnyNet classifier, training would require 4-6 hours, while for the ViT or the RNN, it required around 2 hours.

Greedy community search

For each classifier, we treated the confusion matrix as a weighted graph, allowing us to use theoretical tools from graph theory. To find latent communities based on the classifier's confusion matrix, we implemented Clauset-Newman-Moore greedy modularity maximization. The modularity is calculated

as $Q = \frac{1}{2m}\sum_{ij}(A_{ij} - \gamma\frac{k_i k_j}{2m})\delta(c_i, c_j)$, where m is the number of edges, A is the adjacency matrix, k_i and c_i the weighted degree of node i, γ is the resolution, and $\delta(c_i, c_j)$ equals 1 when i and j are in the same community otherwise equals 0. The greedy-based method begins with each node in the graph as its own community and repeatedly merged the pairs of communities that "lead to the largest modularity until no further increase in modularity is possible (a maximum)". We performed this greedy search under different resolution (γ) conditions. We used the NetworkX package to complete above functions https://networkx.org/.

Funding

This research was funded by CIHR Project Grant RN38364, NSERC Discovery Grant RGPIN-2024-05162 and the Brain Heart Interconnectome's Neuro-AI Platform.

Author Contributions

XW and RN designed the study, interpreted the results and wrote the manuscript. XW performed the computational analyses. JCB and RN acquired funding. RN supervised the project. JCB provided a verification of the approaches.

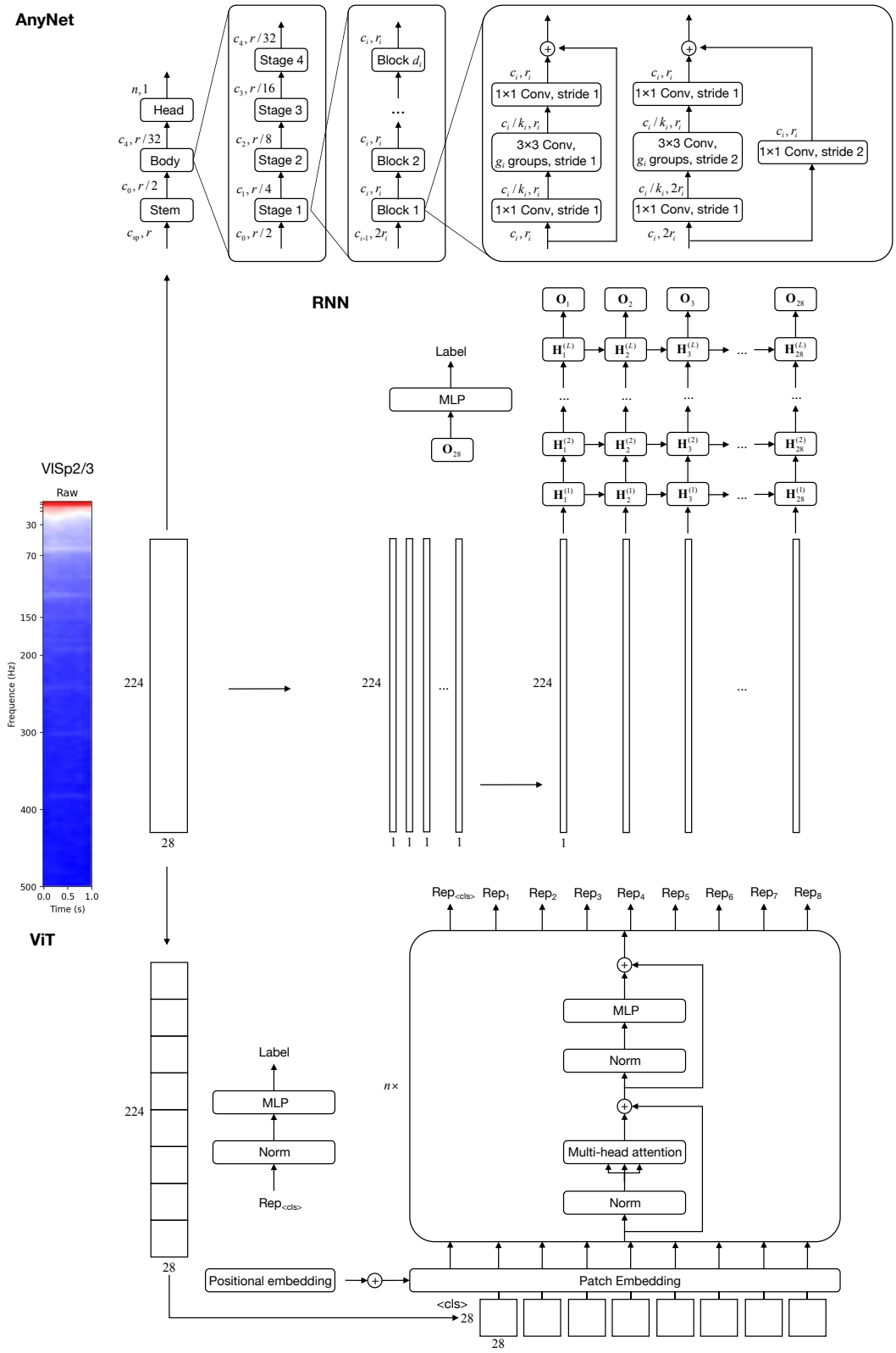

Supplementary Figure 1: **Architectures for the AnyNet, ViT and RNN** As shown above, for AnyNet, the input spectrogram is processed as a image and fed in the classifier; for ViT, the input is separated as several patches for the attention processing; for RNN, the input is cut as temporal slices and given to the classifier sequentially.

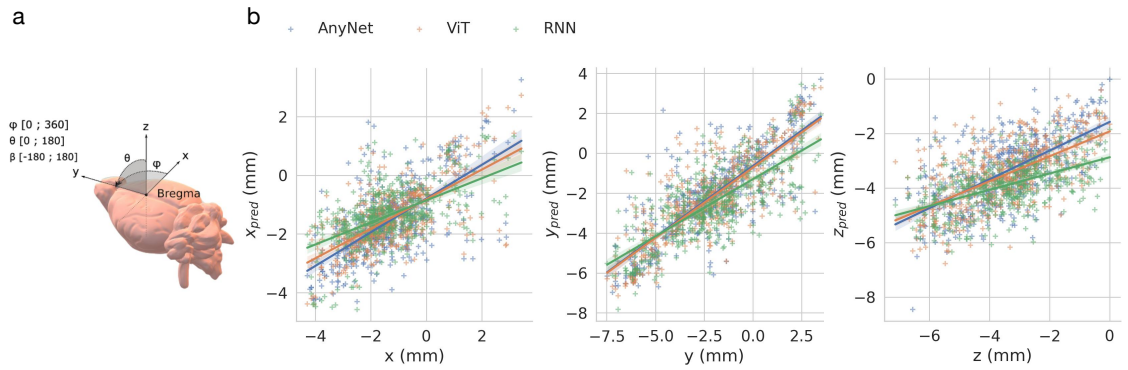

Supplementary Figure 2: **Deep learning-based regression for stereotactic coordinates using LFPs. a.** Illustration of stereotactic coordinates in mouse brain. **b.** Regression for x, y and z axis using LFPs. Deep learning methods, AnyNet, ViT, and RNN are able to predict stereotactic coordinates. For x axis, AnyNet ($R^2 = 0.356, r = 0.656, p < 0.001$), ViT ($R^2 = 0.433, r = 0.672, p < 0.001$), and RNN ($R^2 = 0.2889, r = 0.553, p < 0.001$). For y axis, AnyNet ($R^2 = 0.655, r = 0.812, p < 0.001$), ViT ($R^2 = 0.683, r = 0.828, p < 0.001$), and RNN ($R^2 = 0.527, r = 0.746, p < 0.001$). For z axis, AnyNet ($R^2 = 0.395, r = 0.650, p < 0.001$), ViT ($R^2 = 0.373, r = 0.622, p < 0.001$), RNN ($R^2 = 0.197, r = 0.534, p < 0.001$)

.

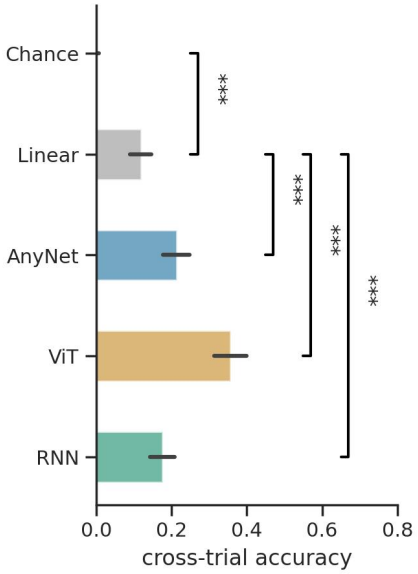

Supplementary Figure 3: **Classification using mean spectrogram of inter-trial state.** Overall cross-trial accuracy from distinct classifiers: linear network model, AnyNet, ViT, and RNN. Linear classifier performs significantly better than the chance level ($p < 0.001$). The three deep networks (AnyNet, ViT, and RNN) outperform the linear classifier ($p < 0.001$). Overall cross-trial accuracy: linear model (0.119), AnyNet (0.213), ViT(0.357), and RNN (0.176).

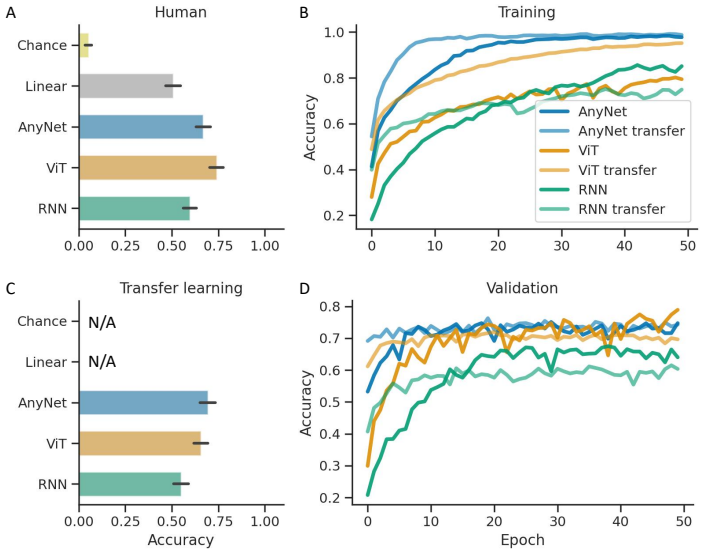

Supplementary Figure 4: **Pre-training on mouse data accelerates training on human data. a.** Overall cross-trial accuracy for the human Neuropixels dataset trained from random initialization. **b.** Training accuracy of three classifiers for the transfer learning and training from the random initialization. **c.** Cross-trial accuracy for the transfer learning of three classifiers. **d.** Validation accuracy curves during training for three classifiers during transfer learning.

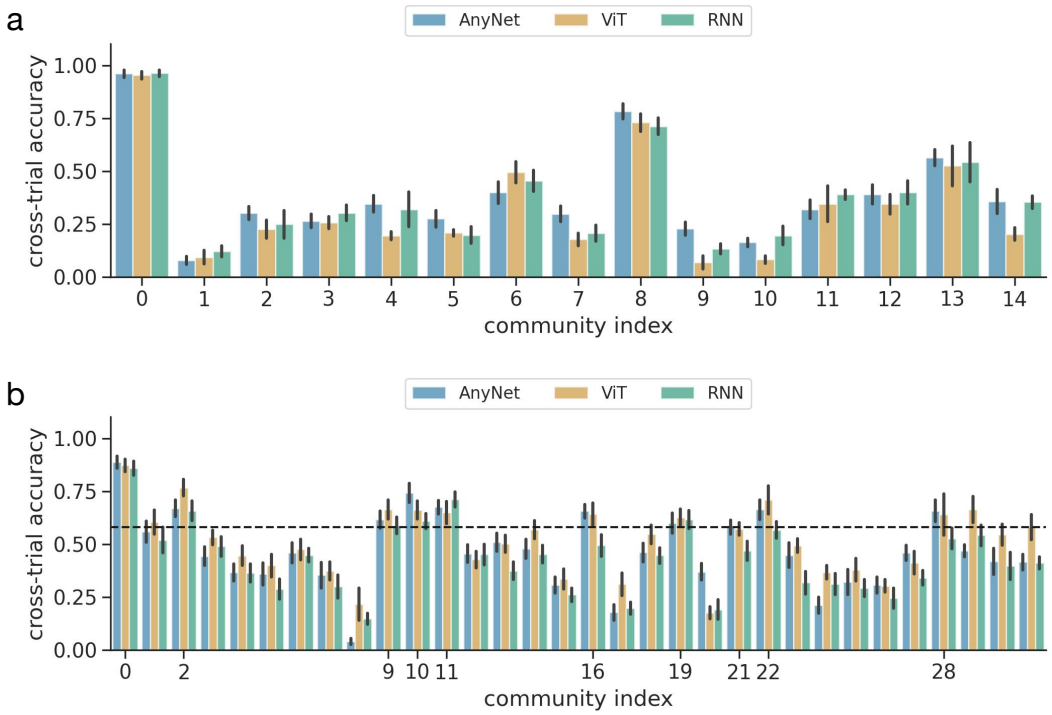

Supplementary Figure 5: **Individual cross-trial accuracy for communities under different resolutions. a.** Individual cross-trial accuracy for communities under 0.4 resolutions. **b.** Individual cross-trial accuracy for communities under 1.0 resolutions. Communities which individual accuracy for AnyNet are in Top 10 (above the dash line) are selected as landmark communities.

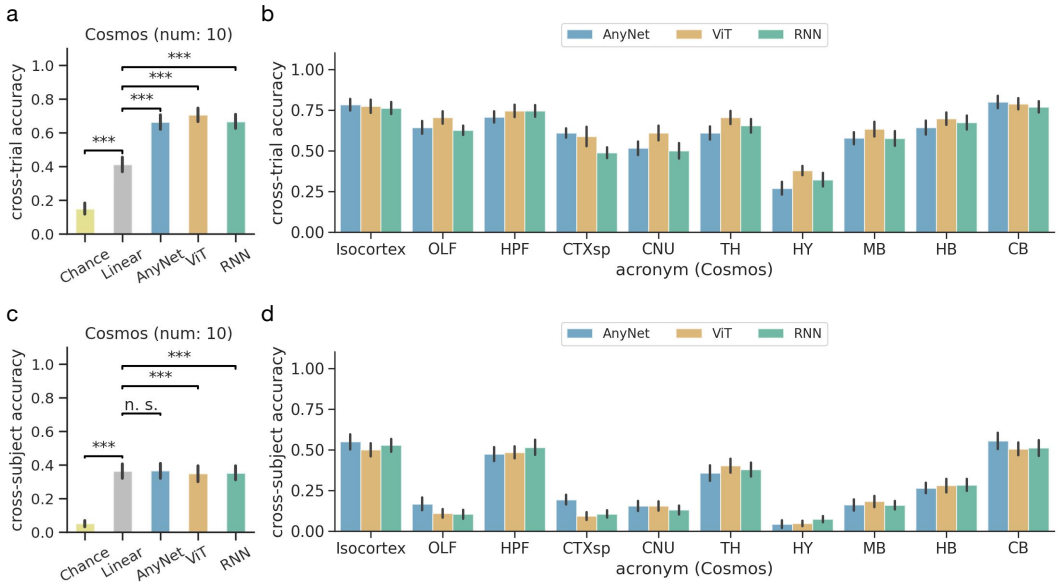

Supplementary Figure 6: **Classification of Cosmos mapping. a.** Overall cross-trial accuracy for Cosmos mapping. **b.** Individual cross-trial accuracy for Cosmos mapping. **c.** Overall cross-subject accuracy for Cosmos mapping. **d.** Individual cross-subject accuracy for Cosmos mapping.

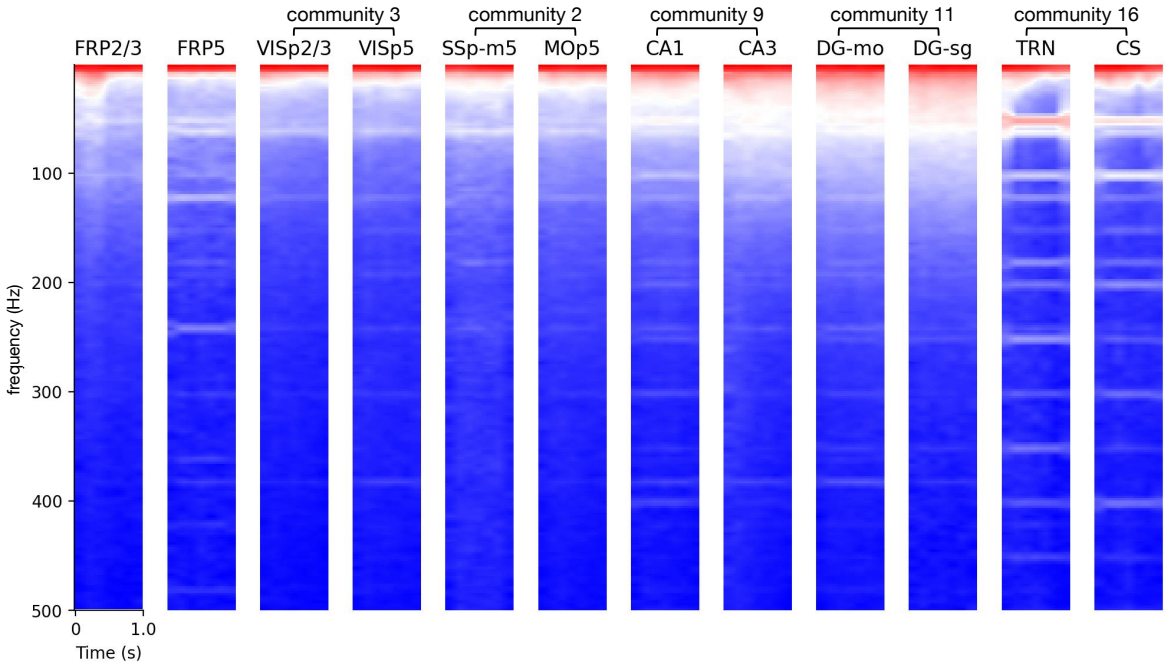

Supplementary Figure 7: **Mean spectrogram of distinct brain areas of inter-trial state.** Power spectra were normalized and read out with a logarithm for visualization. Red means high amplitude; and blue represents low amplitude. Brain areas from the same community are marked. Much of the bar structure seen in, for instance, TRN arises from scaling a lower power signal that contained the alternative current artifact (at 50 Hz for European labs and 60 Hz for American labs) and its harmonics.

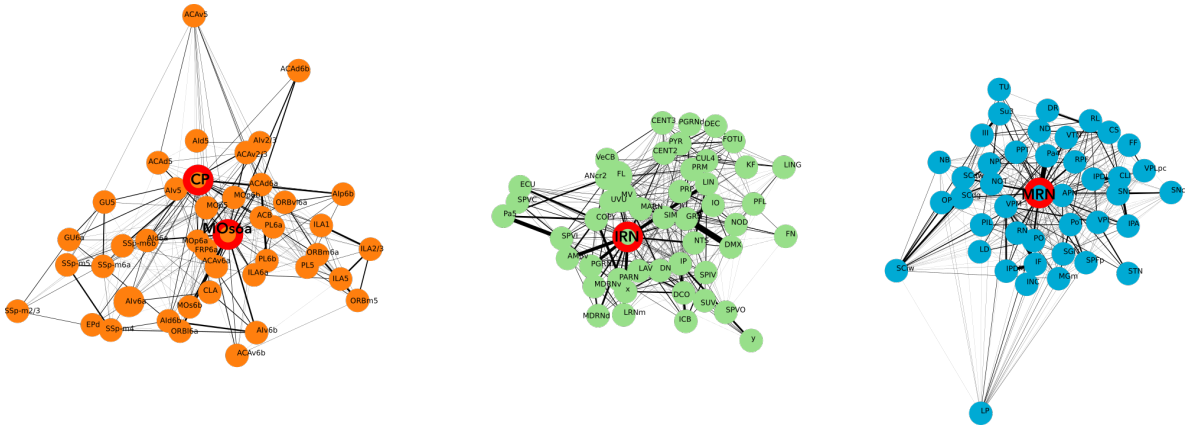

Supplementary Figure 8: **Selection of hub areas.** Three communities where hub areas are highlighted in red : the cortico-basal ganglia loop intertrial period community with caudate putatmen and secondary motor cortex as a hub (left), cerebellum-hindbrain audiovisual cue community with intermediate reticular nucleus as a hub (middle), the oculomotor audiovisual cue community with midbrain reticular nucleus as a hub (right).

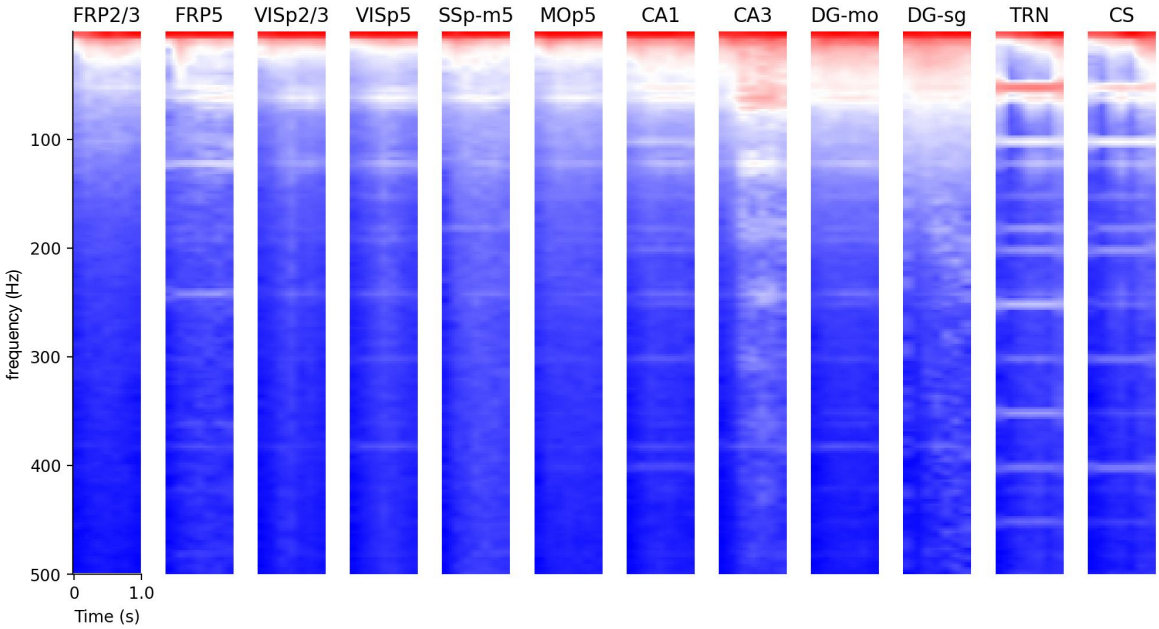

Supplementary Figure 9: **Mean spectrogram of distinct brain areas of task period.** Same as Supplementary Fig. 7 we show the logarithm of the mean spectrogram of task period.

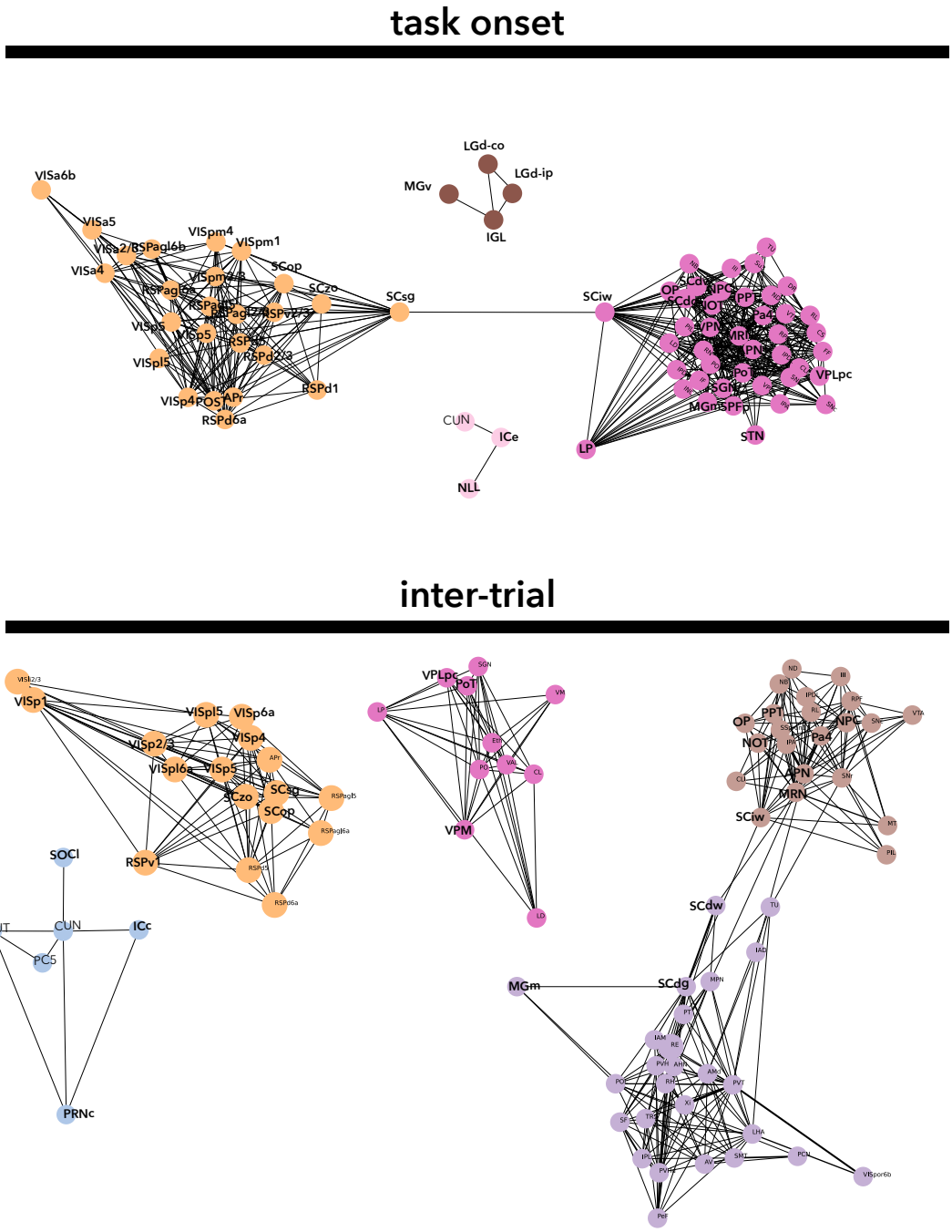

Supplementary Figure 10: **Electrospectral for basic audio-visual areas.** Selection of communities containing areas associated with lower order subcortical visual sensory (lateral geniculate nucleus, LGd, superior colliculus, SCop, SCzo and SCsg), auditory (inferior colliculus ICc, medial geniculate nucleus, MGm, MGv, Nucleus of the Lateral Lemniscus NLL, superior olive SOCl), oculomotor (MRN, APN, Pa4, NOT, IP, PPT, superior colliculus, SCiw, SCdw and SCdg) and auditory reflexes (caudal part of pontine reticular nucleus PRNc) information. Graph links represent thresholded confusion matrix element with line thickness.

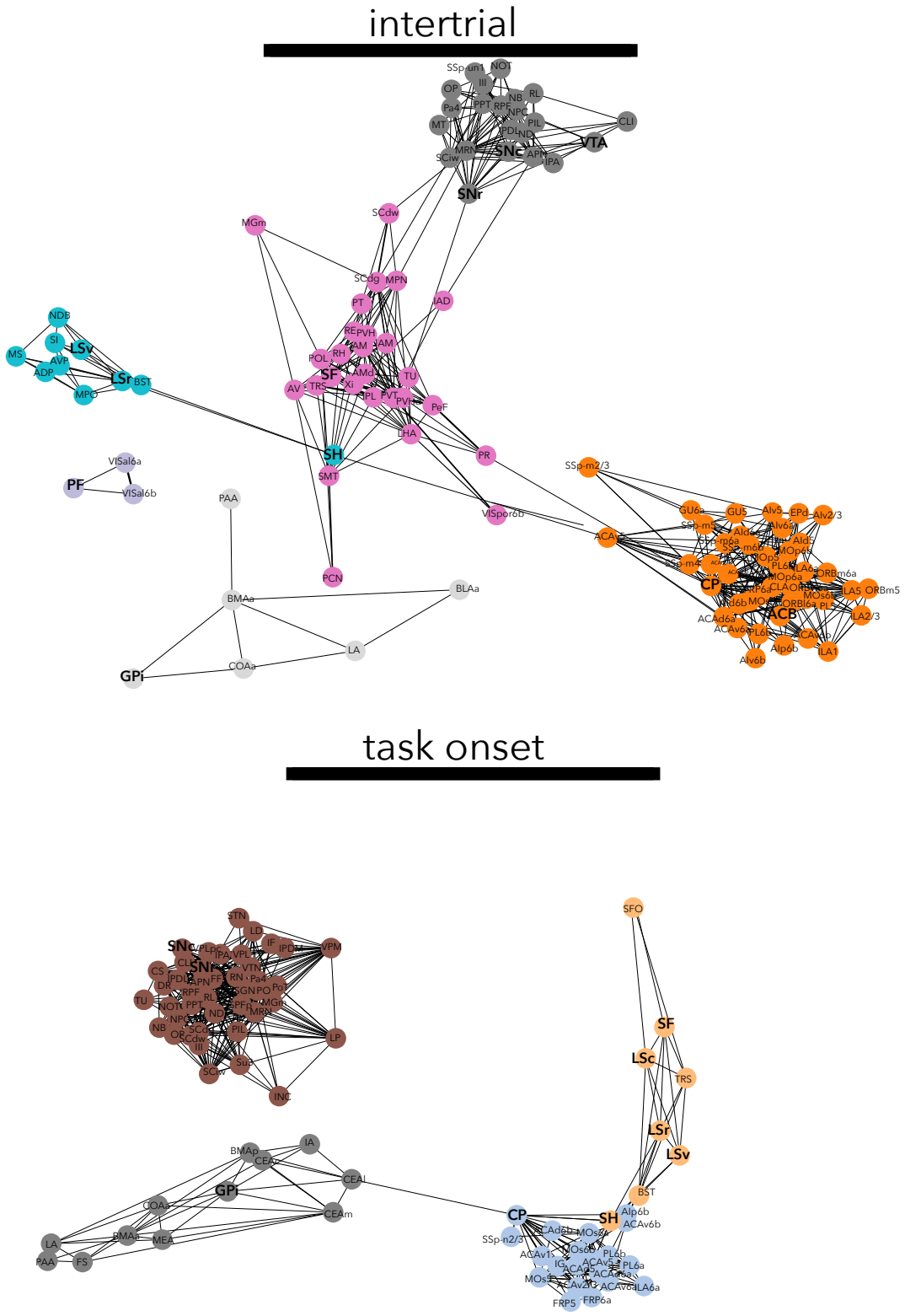

Supplementary Figure 11: **Electrospectral for kinematics system.** Selection of communities containing areas associated with kinematics: putamen (CP), parafasacicular nucleus (PF), lateral septum (LSr, LSv), globus pallidus (GPi), nucleus accumbens (ACB), septofimbrial nucleus (SF), septohippocampal nucleus (SN), Substantia Nigra (SNr, SNc).

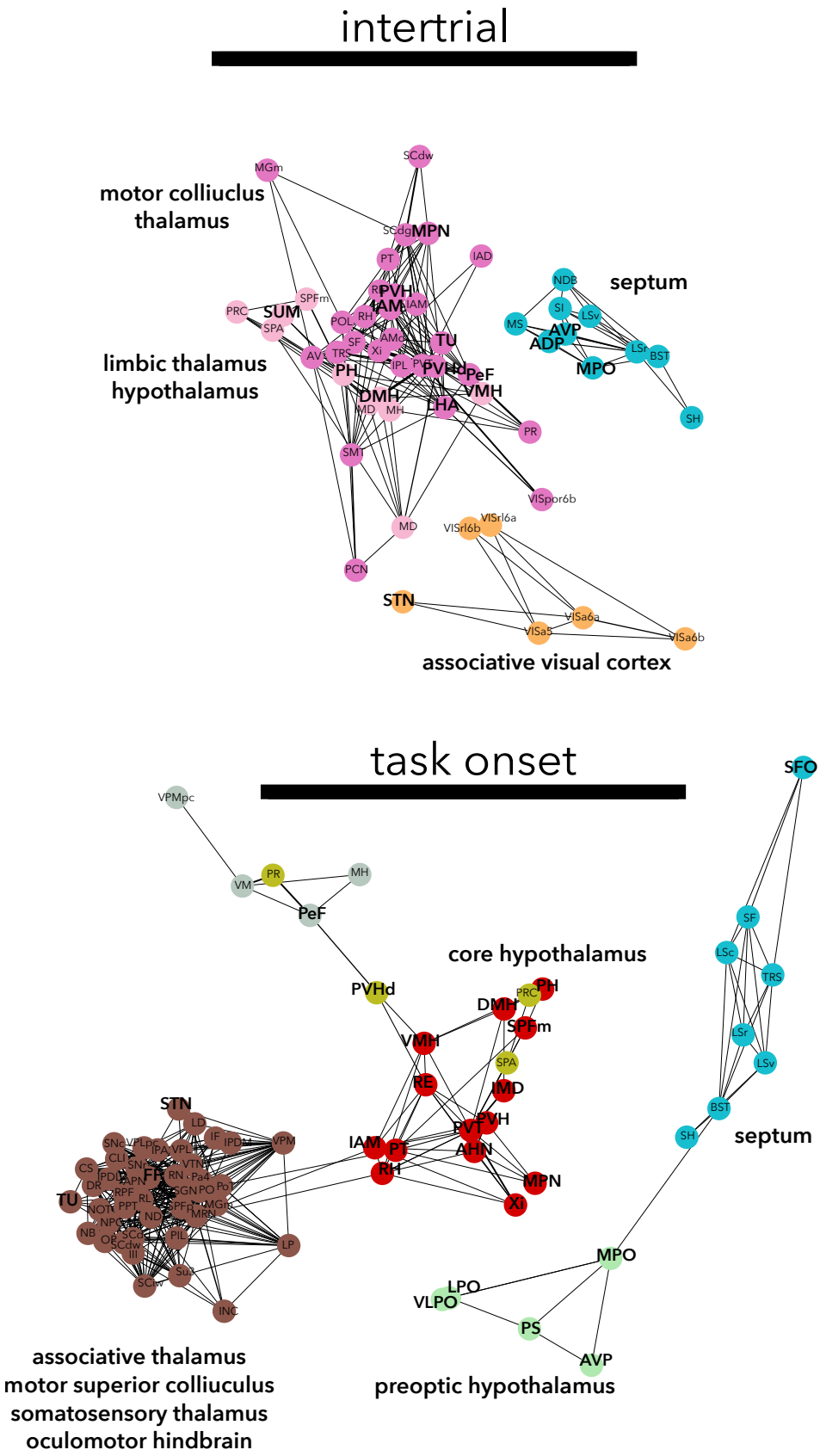

Supplementary Figure 12: **Electrospectral for the hypothalamus.** Selection of communities containing areas that belong to the hypothalamus.

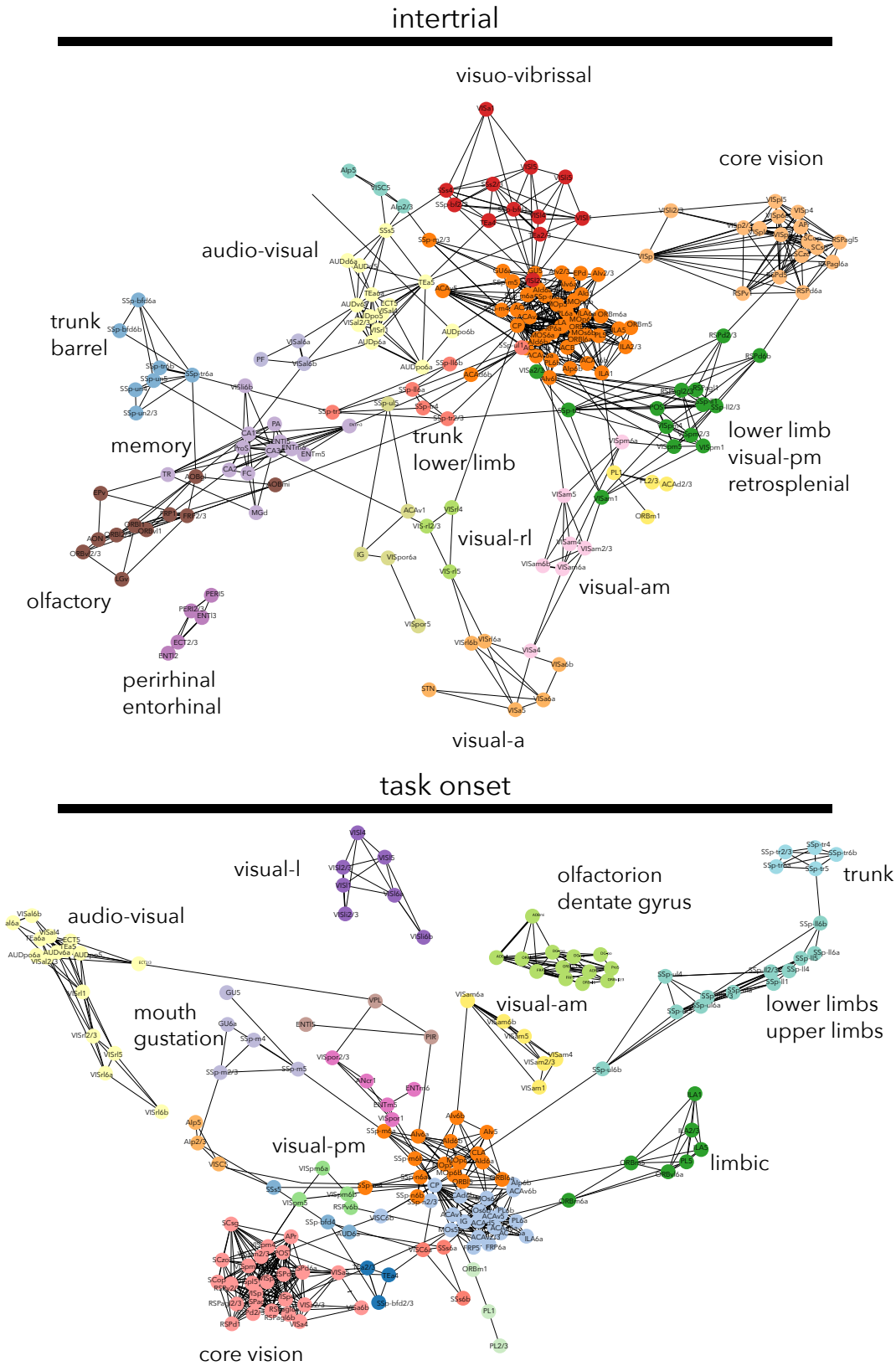

Supplementary Figure 13: **Electrospectral for the cortex.** Selection of communities containing areas that belong to the isocortex.

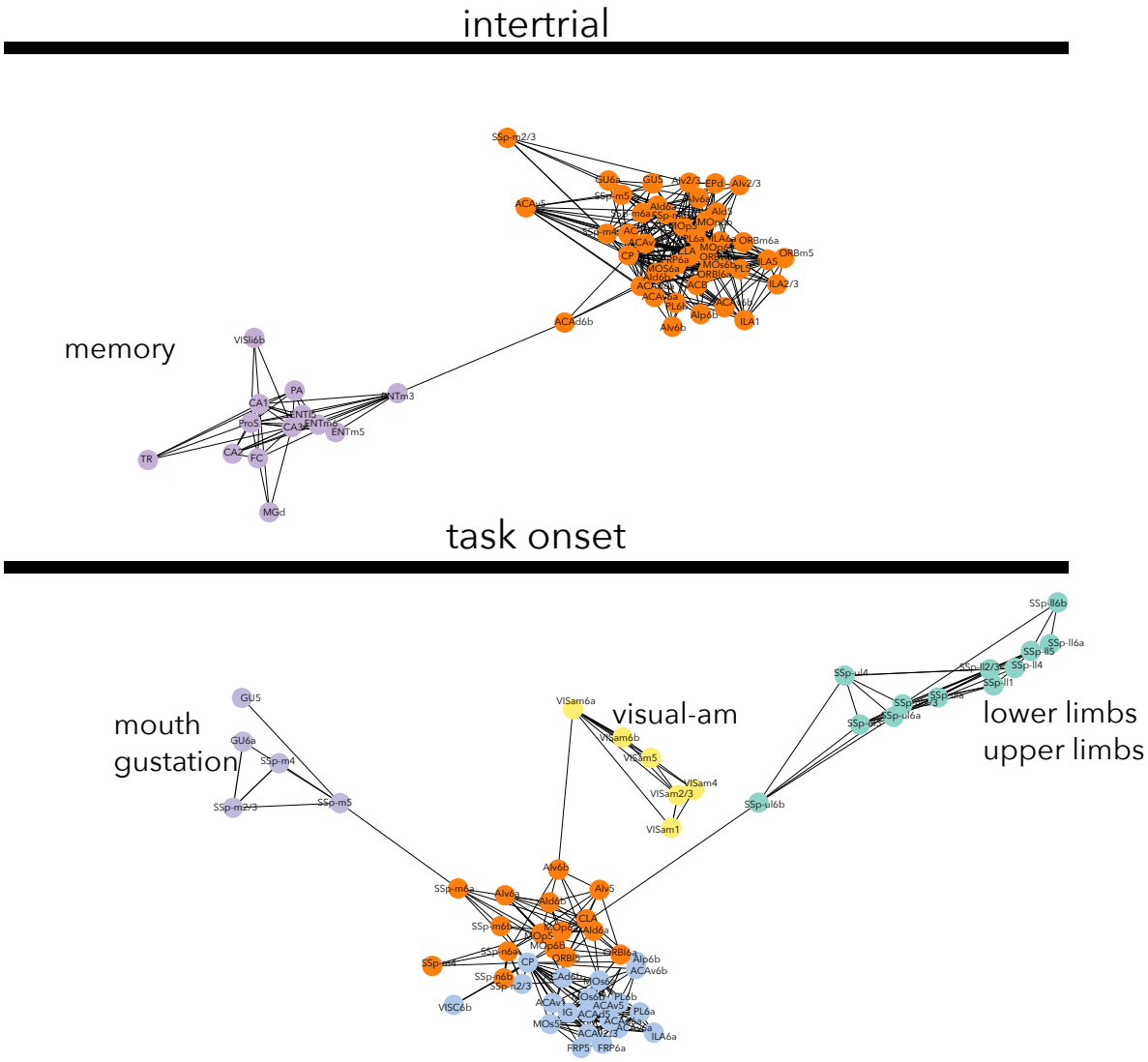

Supplementary Figure 14: **Selection of narrow intercommunity links.** Top: for intertrial communities, the memory community links to the motor planning community through layer 3 of the medial entorhinal cortex (ENTm3) and layer 6b of the anterior cingulate area (ACA6b). Bottom, for the task communities linking to the two motor planning communities, the gustatory community hinges on the layer 5 and 6 of mouth somatosensory cortex, visual-am through layer 6 of anteromedial visual cortex and agranular insular cortex layer 6b. The limbs community links through putamen and somatosensory upper limb layer 6b.

Supplementary Table 1: Table for community labels of each area.

Allen acronym	**Allen name**	**Cosmos acronym**	**Cosmos name**	**Inter-trial**	**Audio-visual cue**
FRP1	Frontal pole layer 1	Isocortex	Isocortex	10	26
FRP2/3	Frontal pole layer 2/3	Isocortex	Isocortex	10	26
FRP5	Frontal pole layer 5	Isocortex	Isocortex	-1	1
FRP6a	Frontal pole layer 6a	Isocortex	Isocortex	2	1
MOp1	Primary motor area Layer 1	Isocortex	Isocortex	-1	-1
MOp2/3	Primary motor area Layer 2/3	Isocortex	Isocortex	-1	-1
MOp5	Primary motor area Layer 5	Isocortex	Isocortex	2	2
MOp6a	Primary motor area Layer 6a	Isocortex	Isocortex	2	2
MOp6b	Primary motor area Layer 6b	Isocortex	Isocortex	2	2
MOs1	Secondary motor area layer 1	Isocortex	Isocortex	-1	-1
MOs2/3	Secondary motor area layer 2/3	Isocortex	Isocortex	-1	-1
MOs5	Secondary motor area layer 5	Isocortex	Isocortex	-1	1
MOs6a	Secondary motor area layer 6a	Isocortex	Isocortex	2	1
MOs6b	Secondary motor area layer 6b	Isocortex	Isocortex	2	1
SSp-n1	Primary somatosensory area nose layer 1	Isocortex	Isocortex	-1	-1
SSp-n2/3	Primary somatosensory area nose layer 2/3	Isocortex	Isocortex	-1	1
SSp-n4	Primary somatosensory area nose layer 4	Isocortex	Isocortex	-1	2
SSp-n5	Primary somatosensory area nose layer 5	Isocortex	Isocortex	-1	-1
SSp-n6a	Primary somatosensory area nose layer 6a	Isocortex	Isocortex	-1	2
SSp-n6b	Primary somatosensory area nose layer 6b	Isocortex	Isocortex	-1	2
SSp-bfd1	Primary somatosensory area barrel field layer 1	Isocortex	Isocortex	6	-1
SSp-bfd2/3	Primary somatosensory area barrel field layer 2/3	Isocortex	Isocortex	6	0
SSp-bfd4	Primary somatosensory area barrel field layer 4	Isocortex	Isocortex	5	24
SSp-bfd5	Primary somatosensory area barrel field layer 5	Isocortex	Isocortex	5	-1
SSp-bfd6a	Primary somatosensory area barrel field layer 6a	Isocortex	Isocortex	24	-1
SSp-bfd6b	Primary somatosensory area barrel field layer 6b	Isocortex	Isocortex	24	-1
SSp-ll1	Primary somatosensory area lower limb layer 1	Isocortex	Isocortex	4	20
SSp-ll2/3	Primary somatosensory area lower limb layer 2/3	Isocortex	Isocortex	4	20
SSp-ll4	Primary somatosensory area lower limb layer 4	Isocortex	Isocortex	-1	20
SSp-ll5	Primary somatosensory area lower limb layer 5	Isocortex	Isocortex	-1	20
SSp-ll6a	Primary somatosensory area lower limb layer 6a	Isocortex	Isocortex	23	20

Allen acronym	Allen name	Cosmos acronym	Cosmos name	Inter-trial	Audio-visual cue
SSp-ll6b	Primary somatosensory area lower limb layer 6b	Isocortex	Isocortex	23	20
SSp-m1	Primary somatosensory area mouth layer 1	Isocortex	Isocortex	-1	-1
SSp-m2/3	Primary somatosensory area mouth layer 2/3	Isocortex	Isocortex	2	22
SSp-m4	Primary somatosensory area mouth layer 4	Isocortex	Isocortex	2	22
SSp-m5	Primary somatosensory area mouth layer 5	Isocortex	Isocortex	2	22
SSp-m6a	Primary somatosensory area mouth layer 6a	Isocortex	Isocortex	2	2
SSp-m6b	Primary somatosensory area mouth layer 6b	Isocortex	Isocortex	2	2
SSp-ul1	Primary somatosensory area upper limb layer 1	Isocortex	Isocortex	23	20
SSp-ul2/3	Primary somatosensory area upper limb layer 2/3	Isocortex	Isocortex	-1	20
SSp-ul4	Primary somatosensory area upper limb layer 4	Isocortex	Isocortex	-1	20
SSp-ul5	Primary somatosensory area upper limb layer 5	Isocortex	Isocortex	17	20
SSp-ul6a	Primary somatosensory area upper limb layer 6a	Isocortex	Isocortex	-1	20
SSp-ul6b	Primary somatosensory area upper limb layer 6b	Isocortex	Isocortex	-1	20
SSp-tr1	Primary somatosensory area trunk layer 1	Isocortex	Isocortex	4	-1
SSp-tr2/3	Primary somatosensory area trunk layer 2/3	Isocortex	Isocortex	23	19
SSp-tr4	Primary somatosensory area trunk layer 4	Isocortex	Isocortex	23	19
SSp-tr5	Primary somatosensory area trunk layer 5	Isocortex	Isocortex	23	19
SSp-tr6a	Primary somatosensory area trunk layer 6a	Isocortex	Isocortex	24	19
SSp-tr6b	Primary somatosensory area trunk layer 6b	Isocortex	Isocortex	24	19
SSp-un1	Primary somatosensory area unassigned layer 1	Isocortex	Isocortex	14	-1
SSp-un2/3	Primary somatosensory area unassigned layer 2/3	Isocortex	Isocortex	24	-1
SSp-un4	Primary somatosensory area unassigned layer 4	Isocortex	Isocortex	24	-1
SSp-un5	Primary somatosensory area unassigned layer 5	Isocortex	Isocortex	24	-1
SSp-un6a	Primary somatosensory area unassigned layer 6a	Isocortex	Isocortex	-1	-1
SSp-un6b	Primary somatosensory area unassigned layer 6b	Isocortex	Isocortex	-1	-1
SSs2/3	Supplemental somatosensory area layer 2/3	Isocortex	Isocortex	6	6

Allen acronym	Allen name	Cosmos acronym	Cosmos name	Inter-trial	Audio-visual cue
SSs4	Supplemental somatosensory area layer 4	Isocortex	Isocortex	6	-1
SSs5	Supplemental somatosensory area layer 5	Isocortex	Isocortex	21	24
SSs6a	Supplemental somatosensory area layer 6a	Isocortex	Isocortex	-1	23
SSs6b	Supplemental somatosensory area layer 6b	Isocortex	Isocortex	-1	23
GU5	Gustatory areas layer 5	Isocortex	Isocortex	2	22
GU6a	Gustatory areas layer 6a	Isocortex	Isocortex	2	22
VISC5	Visceral area layer 5	Isocortex	Isocortex	20	25
VISC6a	Visceral area layer 6a	Isocortex	Isocortex	-1	23
VISC6b	Visceral area layer 6b	Isocortex	Isocortex	-1	1
AUDd2/3	Dorsal auditory area layer 2/3	Isocortex	Isocortex	-1	-1
AUDd4	Dorsal auditory area layer 4	Isocortex	Isocortex	-1	-1
AUDd5	Dorsal auditory area layer 5	Isocortex	Isocortex	21	-1
AUDd6a	Dorsal auditory area layer 6a	Isocortex	Isocortex	21	24
AUDd6b	Dorsal auditory area layer 6b	Isocortex	Isocortex	-1	-1
AUDp4	Primary auditory area layer 4	Isocortex	Isocortex	-1	-1
AUDp5	Primary auditory area layer 5	Isocortex	Isocortex	-1	-1
AUDp6a	Primary auditory area layer 6a	Isocortex	Isocortex	21	-1
AUDpo2/3	Posterior auditory area layer 2/3	Isocortex	Isocortex	-1	-1
AUDpo4	Posterior auditory area layer 4	Isocortex	Isocortex	-1	-1
AUDpo5	Posterior auditory area layer 5	Isocortex	Isocortex	21	21
AUDpo6a	Posterior auditory area layer 6a	Isocortex	Isocortex	21	21
AUDpo6b	Posterior auditory area layer 6b	Isocortex	Isocortex	21	-1
AUDv5	Ventral auditory area layer 5	Isocortex	Isocortex	-1	-1
AUDv6a	Ventral auditory area layer 6a	Isocortex	Isocortex	21	21
AUDv6b	Ventral auditory area layer 6b	Isocortex	Isocortex	-1	-1
VISal2/3	Anterolateral visual area layer 2/3	Isocortex	Isocortex	21	21
VISal4	Anterolateral visual area layer 4	Isocortex	Isocortex	21	21
VISal5	Anterolateral visual area layer 5	Isocortex	Isocortex	-1	-1
VISal6a	Anterolateral visual area layer 6a	Isocortex	Isocortex	22	21
VISal6b	Anterolateral visual area layer 6b	Isocortex	Isocortex	22	21
VISam1	Anteromedial visual area layer 1	Isocortex	Isocortex	4	31
VISam2/3	Anteromedial visual area layer 2/3	Isocortex	Isocortex	27	31
VISam4	Anteromedial visual area layer 4	Isocortex	Isocortex	27	31
VISam5	Anteromedial visual area layer 5	Isocortex	Isocortex	27	31
VISam6a	Anteromedial visual area layer 6a	Isocortex	Isocortex	27	31
VISam6b	Anteromedial visual area layer 6b	Isocortex	Isocortex	27	31
VISl1	Lateral visual area layer 1	Isocortex	Isocortex	6	8
VISl2/3	Lateral visual area layer 2/3	Isocortex	Isocortex	6	8
VISl4	Lateral visual area layer 4	Isocortex	Isocortex	6	8
VISl5	Lateral visual area layer 5	Isocortex	Isocortex	6	8
VISl6a	Lateral visual area layer 6a	Isocortex	Isocortex	-1	8
VISl6b	Lateral visual area layer 6b	Isocortex	Isocortex	-1	-1
VISp1	Primary visual area layer 1	Isocortex	Isocortex	3	7
VISp2/3	Primary visual area layer 2/3	Isocortex	Isocortex	3	6
VISp4	Primary visual area layer 4	Isocortex	Isocortex	3	7
VISp5	Primary visual area layer 5	Isocortex	Isocortex	3	7
VISp6a	Primary visual area layer 6a	Isocortex	Isocortex	3	-1
VISp6b	Primary visual area layer 6b	Isocortex	Isocortex	-1	-1
VISpl1	Posterolateral visual area layer 1	Isocortex	Isocortex	5	-1

Allen acronym	Allen name	Cosmos acronym	Cosmos name	Inter-trial	Audio-visual cue
VISpl2/3	Posterolateral visual area layer 2/3	Isocortex	Isocortex	-1	-1
VISpl4	Posterolateral visual area layer 4	Isocortex	Isocortex	-1	-1
VISpl5	Posterolateral visual area layer 5	Isocortex	Isocortex	3	7
VISpl6a	Posterolateral visual area layer 6a	Isocortex	Isocortex	3	6
VISpm1	posteromedial visual area layer 1	Isocortex	Isocortex	4	7
VISpm2/3	posteromedial visual area layer 2/3	Isocortex	Isocortex	4	7
VISpm4	posteromedial visual area layer 4	Isocortex	Isocortex	4	7
VISpm5	posteromedial visual area layer 5	Isocortex	Isocortex	4	5
VISpm6a	posteromedial visual area layer 6a	Isocortex	Isocortex	27	5
VISpm6b	posteromedial visual area layer 6b	Isocortex	Isocortex	-1	5
VISli2/3	Laterointermediate area layer 2/3	Isocortex	Isocortex	3	8
VISli4	Laterointermediate area layer 4	Isocortex	Isocortex	-1	-1
VISli5	Laterointermediate area layer 5	Isocortex	Isocortex	6	-1
VISli6a	Laterointermediate area layer 6a	Isocortex	Isocortex	8	-1
VISli6b	Laterointermediate area layer 6b	Isocortex	Isocortex	9	8
VISpor1	Postrhinal area layer 1	Isocortex	Isocortex	-1	12
VISpor2/3	Postrhinal area layer 2/3	Isocortex	Isocortex	-1	12
VISpor5	Postrhinal area layer 5	Isocortex	Isocortex	17	-1
VISpor6a	Postrhinal area layer 6a	Isocortex	Isocortex	17	-1
VISpor6b	Postrhinal area layer 6b	Isocortex	Isocortex	12	-1
ACAd2/3	Anterior cingulate area dorsal part layer 2/3	Isocortex	Isocortex	31	-1
ACAd5	Anterior cingulate area dorsal part layer 5	Isocortex	Isocortex	2	1
ACAd6a	Anterior cingulate area dorsal part layer 6a	Isocortex	Isocortex	2	1
ACAd6b	Anterior cingulate area dorsal part layer 6b	Isocortex	Isocortex	2	1
ACAv1	Anterior cingulate area ventral part layer 1	Isocortex	Isocortex	17	1
ACAv2/3	Anterior cingulate area ventral part layer 2/3	Isocortex	Isocortex	2	1
ACAv5	Anterior cingulate area ventral part layer 5	Isocortex	Isocortex	2	1
ACAv6a	Anterior cingulate area ventral part 6a	Isocortex	Isocortex	2	1
ACAv6b	Anterior cingulate area ventral part 6b	Isocortex	Isocortex	2	1
PL1	Prelimbic area layer 1	Isocortex	Isocortex	31	30
PL2/3	Prelimbic area layer 2/3	Isocortex	Isocortex	31	30
PL5	Prelimbic area layer 5	Isocortex	Isocortex	2	4
PL6a	Prelimbic area layer 6a	Isocortex	Isocortex	2	1
PL6b	Prelimbic area layer 6b	Isocortex	Isocortex	2	1
ILA1	Infralimbic area layer 1	Isocortex	Isocortex	2	4
ILA2/3	Infralimbic area layer 2/3	Isocortex	Isocortex	2	4
ILA5	Infralimbic area layer 5	Isocortex	Isocortex	2	4
ILA6a	Infralimbic area layer 6a	Isocortex	Isocortex	2	1
ORBl1	Orbital area lateral part layer 1	Isocortex	Isocortex	10	26
ORBl2/3	Orbital area lateral part layer 2/3	Isocortex	Isocortex	10	26
ORBl5	Orbital area lateral part layer 5	Isocortex	Isocortex	7	2
ORBl6a	Orbital area lateral part layer 6a	Isocortex	Isocortex	2	2
ORBm1	Orbital area medial part layer 1	Isocortex	Isocortex	31	30
ORBm2/3	Orbital area medial part layer 2/3	Isocortex	Isocortex	7	-1

Allen acronym	Allen name	Cosmos acronym	Cosmos name	Inter-trial	Audio-visual cue
ORBm5	Orbital area medial part layer 5	Isocortex	Isocortex	2	4
ORBm6a	Orbital area medial part layer 6a	Isocortex	Isocortex	2	4
ORBvl1	Orbital area ventrolateral part layer 1	Isocortex	Isocortex	10	26
ORBvl2/3	Orbital area ventrolateral part layer 2/3	Isocortex	Isocortex	10	26
ORBvl5	Orbital area ventrolateral part layer 5	Isocortex	Isocortex	-1	-1
ORBvl6a	Orbital area ventrolateral part layer 6a	Isocortex	Isocortex	2	4
AId5	Agranular insular area dorsal part layer 5	Isocortex	Isocortex	2	-1
AId6a	Agranular insular area dorsal part layer 6a	Isocortex	Isocortex	2	2
AId6b	Agranular insular area dorsal part layer 6b	Isocortex	Isocortex	2	2
AIp1	Agranular insular area posterior part layer 1	Isocortex	Isocortex	-1	23
AIp2/3	Agranular insular area posterior part layer 2/3	Isocortex	Isocortex	20	25
AIp5	Agranular insular area posterior part layer 5	Isocortex	Isocortex	20	25
AIp6a	Agranular insular area posterior part layer 6a	Isocortex	Isocortex	-1	-1
AIp6b	Agranular insular area posterior part layer 6b	Isocortex	Isocortex	2	1
AIv2/3	Agranular insular area ventral part layer 2/3	Isocortex	Isocortex	2	-1
AIv5	Agranular insular area ventral part layer 5	Isocortex	Isocortex	2	2
AIv6a	Agranular insular area ventral part layer 6a	Isocortex	Isocortex	2	2
AIv6b	Agranular insular area ventral part layer 6b	Isocortex	Isocortex	2	2
RSPagl1	Retrosplenial area lateral agranular part layer 1	Isocortex	Isocortex	4	-1
RSPagl2/3	Retrosplenial area lateral agranular part layer 2/3	Isocortex	Isocortex	4	7
RSPagl5	Retrosplenial area lateral agranular part layer 5	Isocortex	Isocortex	3	7
RSPagl6a	Retrosplenial area lateral agranular part layer 6a	Isocortex	Isocortex	3	7
RSPagl6b	Retrosplenial area lateral agranular part layer 6b	Isocortex	Isocortex	-1	7
RSPd1	Retrosplenial area dorsal part layer 1	Isocortex	Isocortex	-1	7
RSPd2/3	Retrosplenial area dorsal part layer 2/3	Isocortex	Isocortex	4	7
RSPd5	Retrosplenial area dorsal part layer 5	Isocortex	Isocortex	3	7
RSPd6a	Retrosplenial area dorsal part layer 6a	Isocortex	Isocortex	3	7

Allen acronym	Allen name	Cosmos acronym	Cosmos name	Inter-trial	Audio-visual cue
RSPd6b	Retrosplenial area dorsal part layer 6b	Isocortex	Isocortex	4	5
RSPv1	Retrosplenial area ventral part layer 1	Isocortex	Isocortex	3	-1
RSPv2/3	Retrosplenial area ventral part layer 2/3	Isocortex	Isocortex	-1	7
RSPv5	Retrosplenial area ventral part layer 5	Isocortex	Isocortex	-1	-1
RSPv6a	Retrosplenial area ventral part layer 6a	Isocortex	Isocortex	-1	6
RSPv6b	Retrosplenial area ventral part layer 6b	Isocortex	Isocortex	-1	5
VISa1	Anterior area layer 1	Isocortex	Isocortex	6	-1
VISa2/3	Anterior area layer 2/3	Isocortex	Isocortex	4	7
VISa4	Anterior area layer 4	Isocortex	Isocortex	27	7
VISa5	Anterior area layer 5	Isocortex	Isocortex	25	7
VISa6a	Anterior area layer 6a	Isocortex	Isocortex	25	-1
VISa6b	Anterior area layer 6b	Isocortex	Isocortex	25	7
VISrl1	Rostrolateral area layer 1	Isocortex	Isocortex	21	21
VISrl2/3	Rostrolateral area layer 2/3	Isocortex	Isocortex	26	21
VISrl4	Rostrolateral area layer 4	Isocortex	Isocortex	26	-1
VISrl5	Rostrolateral area layer 5	Isocortex	Isocortex	26	21
VISrl6a	Rostrolateral area layer 6a	Isocortex	Isocortex	25	21
VISrl6b	Rostrolateral area layer 6b	Isocortex	Isocortex	25	21
TEa2/3	Temporal association areas layer 2/3	Isocortex	Isocortex	6	0
TEa4	Temporal association areas layer 4	Isocortex	Isocortex	6	0
TEa5	Temporal association areas layer 5	Isocortex	Isocortex	21	21
TEa6a	Temporal association areas layer 6a	Isocortex	Isocortex	21	21
TEa6b	Temporal association areas layer 6b	Isocortex	Isocortex	8	-1
PERI1	Perirhinal area layer 1	Isocortex	Isocortex	-1	-1
PERI2/3	Perirhinal area layer 2/3	Isocortex	Isocortex	29	-1
PERI5	Perirhinal area layer 5	Isocortex	Isocortex	29	-1
ECT2/3	Ectorhinal area/Layer 2/3	Isocortex	Isocortex	29	21
ECT5	Ectorhinal area/Layer 5	Isocortex	Isocortex	21	21
ECT6a	Ectorhinal area/Layer 6a	Isocortex	Isocortex	-1	-1
ECT6b	Ectorhinal area/Layer 6b	Isocortex	Isocortex	-1	-1
AOBgl	Accessory olfactory bulb glomerular layer	OLF	Olfactory areas	10	26
AOBmi	Accessory olfactory bulb mitral layer	OLF	Olfactory areas	10	26
DG-mo	Dentate gyrus molecular layer	HPF	Hippocampal formation	11	26
DG-po	Dentate gyrus polymorph layer	HPF	Hippocampal formation	11	26
DG-sg	Dentate gyrus granule cell layer	HPF	Hippocampal formation	11	26
FC	Fasciola cinerea	HPF	Hippocampal formation	9	-1
IG	Induseum griseum	HPF	Hippocampal formation	17	1
ENTl1	Entorhinal area lateral part layer 1	HPF	Hippocampal formation	-1	-1

Allen acronym	Allen name	Cosmos acronym	Cosmos name	Inter-trial	Audio-visual cue
ENTl2	Entorhinal area lateral part layer 2	HPF	Hippocampal formation	29	-1
ENTl3	Entorhinal area lateral part layer 3	HPF	Hippocampal formation	29	11
ENTl5	Entorhinal area lateral part layer 5	HPF	Hippocampal formation	9	11
ENTl6a	Entorhinal area lateral part layer 6a	HPF	Hippocampal formation	-1	-1
ENTm1	Entorhinal area medial part dorsal zone layer 1	HPF	Hippocampal formation	-1	-1
ENTm2	Entorhinal area medial part dorsal zone layer 2	HPF	Hippocampal formation	-1	-1
ENTm3	Entorhinal area medial part dorsal zone layer 3	HPF	Hippocampal formation	9	-1
ENTm5	Entorhinal area medial part dorsal zone layer 5	HPF	Hippocampal formation	9	12
ENTm6	Entorhinal area medial part dorsal zone layer 6	HPF	Hippocampal formation	9	12
HATA	Hippocampo-amygdalar transition area	HPF	Hippocampal formation	-1	34
APr	Area prostriata	HPF	Hippocampal formation	3	7
CLA	Claustrum	CTXsp	Cortical subplate	2	2
EPd	Endopiriform nucleus dorsal part	CTXsp	Cortical subplate	2	-1
EPv	Endopiriform nucleus ventral part	CTXsp	Cortical subplate	10	13
LA	Lateral amygdalar nucleus	CTXsp	Cortical subplate	28	14
BLAa	Basolateral amygdalar nucleus anterior part	CTXsp	Cortical subplate	28	-1
BLAp	Basolateral amygdalar nucleus posterior part	CTXsp	Cortical subplate	-1	13
BLAv	Basolateral amygdalar nucleus ventral part	CTXsp	Cortical subplate	-1	-1
BMAa	Basomedial amygdalar nucleus anterior part	CTXsp	Cortical subplate	28	14
BMAp	Basomedial amygdalar nucleus posterior part	CTXsp	Cortical subplate	-1	14
PA	Posterior amygdalar nucleus	CTXsp	Cortical subplate	9	-1
CP	Caudoputamen	CNU	Cerebral nuclei	2	1
ACB	Nucleus accumbens	CNU	Cerebral nuclei	2	-1
FS	Fundus of striatum	CNU	Cerebral nuclei	-1	14
LSc	Lateral septal nucleus caudal (caudodorsal) part	CNU	Cerebral nuclei	-1	3
LSr	Lateral septal nucleus rostral (rostroventral) part	CNU	Cerebral nuclei	18	3

Allen acronym	Allen name	Cosmos acronym	Cosmos name	Inter-trial	Audio-visual cue
LSv	Lateral septal nucleus ventral part	CNU	Cerebral nuclei	18	3
SF	Septofimbrial nucleus	CNU	Cerebral nuclei	12	3
SH	Septohippocampal nucleus	CNU	Cerebral nuclei	18	3
AAA	Anterior amygdalar area	CNU	Cerebral nuclei	-1	-1
CEAc	Central amygdalar nucleus capsular part	CNU	Cerebral nuclei	-1	14
CEAl	Central amygdalar nucleus lateral part	CNU	Cerebral nuclei	-1	14
CEAm	Central amygdalar nucleus medial part	CNU	Cerebral nuclei	-1	14
IA	Intercalated amygdalar nucleus	CNU	Cerebral nuclei	-1	14
GPe	Globus pallidus external segment	CNU	Cerebral nuclei	-1	-1
GPi	Globus pallidus internal segment	CNU	Cerebral nuclei	28	14
SI	Substantia innominata	CNU	Cerebral nuclei	18	-1
MA	Magnocellular nucleus	CNU	Cerebral nuclei	-1	-1
MS	Medial septal nucleus	CNU	Cerebral nuclei	18	-1
NDB	Diagonal band nucleus	CNU	Cerebral nuclei	18	-1
TRS	Triangular nucleus of septum	CNU	Cerebral nuclei	12	3
VAL	Ventral anterior-lateral complex of the thalamus	TH	Thalamus	19	17
VM	Ventral medial nucleus of the thalamus	TH	Thalamus	19	18
VPL	Ventral posterolateral nucleus of the thalamus	TH	Thalamus	-1	10
VPLpc	Ventral posterolateral nucleus of the thalamus parvicellular part	TH	Thalamus	19	10
VPM	Ventral posteromedial nucleus of the thalamus	TH	Thalamus	19	10
VPMpc	Ventral posteromedial nucleus of the thalamus parvicellular part	TH	Thalamus	-1	18
PoT	Posterior triangular thalamic nucleus	TH	Thalamus	19	10
SPFm	Subparafascicular nucleus magnocellular part	TH	Thalamus	13	15
SPFp	Subparafascicular nucleus parvicellular part	TH	Thalamus	-1	10
SPA	Subparafascicular area	TH	Thalamus	13	16
PP	Peripeduncular nucleus	TH	Thalamus	-1	-1
MGd	Medial geniculate complex dorsal part	TH	Thalamus	9	-1

Allen acronym	Allen name	Cosmos acronym	Cosmos name	Inter-trial	Audio-visual cue
MGv	Medial geniculate complex ventral part	TH	Thalamus	-1	29
MGm	Medial geniculate complex medial part	TH	Thalamus	12	10
LGd-sh	Dorsal part of the lateral geniculate complex shell	TH	Thalamus	-1	-1
LGd-co	Dorsal part of the lateral geniculate complex core	TH	Thalamus	-1	29
LGd-ip	Dorsal part of the lateral geniculate complex ipsilateral zone	TH	Thalamus	-1	29
LP	Lateral posterior nucleus of the thalamus	TH	Thalamus	19	10
PO	Posterior complex of the thalamus	TH	Thalamus	19	10
POL	Posterior limiting nucleus of the thalamus	TH	Thalamus	12	-1
SGN	Suprageniculate nucleus	TH	Thalamus	19	10
Eth	Ethmoid nucleus of the thalamus	TH	Thalamus	19	-1
AV	Anteroventral nucleus of thalamus	TH	Thalamus	12	17
AMd	Anteromedial nucleus dorsal part	TH	Thalamus	12	-1
AMv	Anteromedial nucleus ventral part	TH	Thalamus	-1	-1
AD	Anterodorsal nucleus	TH	Thalamus	-1	-1
IAM	Interanteromedial nucleus of the thalamus	TH	Thalamus	12	15
IAD	Interanterodorsal nucleus of the thalamus	TH	Thalamus	12	-1
LD	Lateral dorsal nucleus of thalamus	TH	Thalamus	19	10
IMD	Intermediodorsal nucleus of the thalamus	TH	Thalamus	13	15
SMT	Submedial nucleus of the thalamus	TH	Thalamus	12	17
PR	Perireunensis nucleus	TH	Thalamus	12	16
PVT	Paraventricular nucleus of the thalamus	TH	Thalamus	12	15
PT	Parataenial nucleus	TH	Thalamus	12	15
RE	Nucleus of reuniens	TH	Thalamus	12	15
Xi	Xiphoid thalamic nucleus	TH	Thalamus	12	15
RH	Rhomboid nucleus	TH	Thalamus	12	15
CM	Central medial nucleus of the thalamus	TH	Thalamus	-1	-1
PCN	Paracentral nucleus	TH	Thalamus	12	17
CL	Central lateral nucleus of the thalamus	TH	Thalamus	19	-1
PF	Parafascicular nucleus	TH	Thalamus	22	-1
PIL	Posterior intralaminar thalamic nucleus	TH	Thalamus	14	10
RT	Reticular nucleus of the thalamus	TH	Thalamus	-1	-1
IGL	Intergeniculate leaflet of the lateral geniculate complex	TH	Thalamus	-1	29
IntG	Intermediate geniculate nucleus	TH	Thalamus	-1	-1
SubG	Subgeniculate nucleus	TH	Thalamus	-1	-1
MH	Medial habenula	TH	Thalamus	13	18
LH	Lateral habenula	TH	Thalamus	-1	-1
ADP	Anterodorsal preoptic nucleus	HY	Hypothalamus	18	-1
AVP	Anteroventral preoptic nucleus	HY	Hypothalamus	18	33

Allen acronym	Allen name	Cosmos acronym	Cosmos name	Inter-trial	Audio-visual cue
MPO	Medial preoptic area	HY	Hypothalamus	18	33
PS	Parastrial nucleus	HY	Hypothalamus	-1	33
SFO	Subfornical organ	HY	Hypothalamus	-1	3
VLPO	Ventrolateral preoptic nucleus	HY	Hypothalamus	-1	33
LM	Lateral mammillary nucleus	HY	Hypothalamus	-1	-1
Mml	Medial mammillary nucleus lateral part	HY	Hypothalamus	-1	-1
PH	Posterior hypothalamic nucleus	HY	Hypothalamus	13	15
LHA	Lateral hypothalamic area	HY	Hypothalamus	12	-1
LPO	Lateral preoptic area	HY	Hypothalamus	-1	33
PeF	Perifornical nucleus	HY	Hypothalamus	12	18
STN	Subthalamic nucleus	HY	Hypothalamus	25	10
TU	Tuberal nucleus	HY	Hypothalamus	12	10
FF	Fields of Forel	HY	Hypothalamus	-1	10
SCop	Superior colliculus optic layer	MB	Midbrain	3	7
SCsg	Superior colliculus superficial gray layer	MB	Midbrain	3	7
SCzo	Superior colliculus zonal layer	MB	Midbrain	3	7
ICc	Inferior colliculus central nucleus	MB	Midbrain	1	-1
ICd	Inferior colliculus dorsal nucleus	MB	Midbrain	-1	-1
ICe	Inferior colliculus external nucleus	MB	Midbrain	-1	27
NB	Nucleus of the brachium of the inferior colliculus	MB	Midbrain	14	10
SAG	Nucleus sagulum	MB	Midbrain	-1	-1
PBG	Parabigeminal nucleus	MB	Midbrain	-1	-1
SNr	Substantia nigra reticular part	MB	Midbrain	14	10
VTA	Ventral tegmental area	MB	Midbrain	14	-1
RR	Midbrain reticular nucleus retrorubral area	MB	Midbrain	-1	-1
SCdg	Superior colliculus motor related deep gray layer	MB	Midbrain	12	10
SCdw	Superior colliculus motor related deep white layer	MB	Midbrain	12	10
SCiw	Superior colliculus motor related intermediate white layer	MB	Midbrain	14	10
PRC	Precommissural nucleus	MB	Midbrain	13	16
INC	Interstitial nucleus of Cajal	MB	Midbrain	-1	10
ND	Nucleus of Darkschewitsch	MB	Midbrain	14	10
Su3	Supraoculomotor periaqueductal gray	MB	Midbrain	-1	10
APN	Anterior pretectal nucleus	MB	Midbrain	14	10
MPT	Medial pretectal area	MB	Midbrain	-1	-1
NOT	Nucleus of the optic tract	MB	Midbrain	14	10
NPC	Nucleus of the posterior commissure	MB	Midbrain	14	10
OP	Olivary pretectal nucleus	MB	Midbrain	14	10
PPT	Posterior pretectal nucleus	MB	Midbrain	14	10
RPF	Retroparafascicular nucleus	MB	Midbrain	14	10
CUN	Cuneiform nucleus	MB	Midbrain	1	27
RN	Red nucleus	MB	Midbrain	15	10
III	Oculomotor nucleus	MB	Midbrain	14	10
MA3	Medial accesory oculomotor nucleus	MB	Midbrain	-1	-1
EW	Edinger-Westphal nucleus	MB	Midbrain	-1	-1
Pa4	Paratrochlear nucleus	MB	Midbrain	14	10

Allen acronym	Allen name	Cosmos acronym	Cosmos name	Inter-trial	Audio-visual cue
VTN	Ventral tegmental nucleus	MB	Midbrain	15	10
AT	Anterior tegmental nucleus	MB	Midbrain	16	32
DT	Dorsal terminal nucleus of the accessory optic tract	MB	Midbrain	8	-1
MT	Medial terminal nucleus of the accessory optic tract	MB	Midbrain	14	-1
SNc	Substantia nigra compact part	MB	Midbrain	14	10
PPN	Pedunculopontine nucleus	MB	Midbrain	-1	-1
IF	Interfascicular nucleus raphe	MB	Midbrain	15	10
IPA	Interpeduncular nucleus apical	MB	Midbrain	14	10
IPL	Interpeduncular nucleus lateral	MB	Midbrain	12	-1
IPDM	Interpeduncular nucleus dorsomedial	MB	Midbrain	15	10
IPDL	Interpeduncular nucleus dorsolateral	MB	Midbrain	14	10
RL	Rostral linear nucleus raphe	MB	Midbrain	14	10
CLI	Central linear nucleus raphe	MB	Midbrain	14	10
DR	Dorsal nucleus raphe	MB	Midbrain	-1	10
PSV	Principal sensory nucleus of the trigeminal	HB	Hindbrain	-1	28
KF	Koelliker-Fuse subnucleus	HB	Hindbrain	0	9
POR	Superior olivary complex periolivary region	HB	Hindbrain	-1	-1
SOCm	Superior olivary complex medial part	HB	Hindbrain	-1	32
SOCl	Superior olivary complex lateral part	HB	Hindbrain	1	-1
DTN	Dorsal tegmental nucleus	HB	Hindbrain	-1	-1
PDTg	Posterodorsal tegmental nucleus	HB	Hindbrain	-1	-1
PCG	Pontine central gray	HB	Hindbrain	-1	-1
PG	Pontine gray	HB	Hindbrain	-1	-1
PRNc	Pontine reticular nucleus caudal part	HB	Hindbrain	1	-1
SUT	Supratrigeminal nucleus	HB	Hindbrain	1	28
TRN	Tegmental reticular nucleus	HB	Hindbrain	16	-1
V	Motor nucleus of trigeminal	HB	Hindbrain	-1	28
P5	Peritrigeminal zone	HB	Hindbrain	-1	-1
PC5	Parvicellular motor 5 nucleus	HB	Hindbrain	1	28
I5	Intertrigeminal nucleus	HB	Hindbrain	0	-1
LC	Locus ceruleus	HB	Hindbrain	-1	-1
LDT	Laterodorsal tegmental nucleus	HB	Hindbrain	-1	-1
NI	Nucleus incertus	HB	Hindbrain	-1	-1
PRNr	Pontine reticular nucleus	HB	Hindbrain	-1	32
DCO	Dorsal cochlear nucleus	HB	Hindbrain	0	9
VCO	Ventral cochlear nucleus	HB	Hindbrain	0	-1
CU	Cuneate nucleus	HB	Hindbrain	0	-1
ECU	External cuneate nucleus	HB	Hindbrain	0	9
SPVC	Spinal nucleus of the trigeminal caudal part	HB	Hindbrain	0	9
SPVI	Spinal nucleus of the trigeminal interpolar part	HB	Hindbrain	0	9
Pa5	Paratrigeminal nucleus	HB	Hindbrain	0	9
VII	Facial motor nucleus	HB	Hindbrain	-1	-1

Allen acronym	Allen name	Cosmos acronym	Cosmos name	Inter-trial	Audio-visual cue
AMBv	Nucleus ambiguus ventral division	HB	Hindbrain	0	9
DMX	Dorsal motor nucleus of the vagus nerve	HB	Hindbrain	-1	9
GRN	Gigantocellular reticular nucleus	HB	Hindbrain	0	9
ICB	Infracerebellar nucleus	HB	Hindbrain	0	9
IO	Inferior olivary complex	HB	Hindbrain	0	9
IRN	Intermediate reticular nucleus	HB	Hindbrain	0	9
LIN	Linear nucleus of the medulla	HB	Hindbrain	0	9
LRNm	Lateral reticular nucleus magnocellular part	HB	Hindbrain	0	9
MARN	Magnocellular reticular nucleus	HB	Hindbrain	0	9
MDRNd	Medullary reticular nucleus dorsal part	HB	Hindbrain	0	9
MDRNv	Medullary reticular nucleus ventral part	HB	Hindbrain	0	9
PARN	Parvicellular reticular nucleus	HB	Hindbrain	0	9
PAS	Parasolitary nucleus	HB	Hindbrain	0	-1
PGRNd	Paragigantocellular reticular nucleus dorsal part	HB	Hindbrain	0	9
PGRNl	Paragigantocellular reticular nucleus lateral part	HB	Hindbrain	0	9
PRP	Nucleus prepositus	HB	Hindbrain	0	9
LAV	Lateral vestibular nucleus	HB	Hindbrain	0	9
MV	Medial vestibular nucleus	HB	Hindbrain	0	9
SPIV	Spinal vestibular nucleus	HB	Hindbrain	0	9
SUV	Superior vestibular nucleus	HB	Hindbrain	-1	9
x	Nucleus x	HB	Hindbrain	0	9
XII	Hypoglossal nucleus	HB	Hindbrain	30	34
y	Nucleus y	HB	Hindbrain	0	9
RO	Nucleus raphe obscurus	HB	Hindbrain	30	34
FN	Fastigial nucleus	CB	Cerebellum	0	9
IP	Interposed nucleus	CB	Cerebellum	0	9
DN	Dentate nucleus	CB	Cerebellum	0	9
VeCB	Vestibulocerebellar nucleus	CB	Cerebellum	0	9
MOB	Main olfactory bulb	OLF	Olfactory areas	-1	-1
AON	Anterior olfactory nucleus	OLF	Olfactory areas	10	26
TTd	Taenia tecta dorsal part	OLF	Olfactory areas	-1	-1
TTv	Taenia tecta ventral part	OLF	Olfactory areas	-1	-1
DP	Dorsal peduncular area	OLF	Olfactory areas	7	-1
PIR	Piriform area	OLF	Olfactory areas	-1	11
COAa	Cortical amygdalar area anterior part	OLF	Olfactory areas	28	14
COAp	Cortical amygdalar area posterior part	OLF	Olfactory areas	-1	-1
PAA	Piriform-amygdalar area	OLF	Olfactory areas	28	14

Allen acronym	Allen name	Cosmos acronym	Cosmos name	Inter-trial	Audio-visual cue
TR	Postpiriform transition area	OLF	Olfactory areas	9	13
CA1	Field CA1	HPF	Hippocampal formation	9	-1
CA2	Field CA2	HPF	Hippocampal formation	9	-1
CA3	Field CA3	HPF	Hippocampal formation	9	-1
PAR	Parasubiculum	HPF	Hippocampal formation	-1	-1
POST	Postsubiculum	HPF	Hippocampal formation	4	7
PRE	Presubiculum	HPF	Hippocampal formation	-1	-1
SUB	Subiculum	HPF	Hippocampal formation	-1	-1
ProS	Prosubiculum	HPF	Hippocampal formation	9	26
OT	Olfactory tubercle	CNU	Cerebral nuclei	-1	-1
MEA	Medial amygdalar nucleus	CNU	Cerebral nuclei	-1	14
BST	Bed nuclei of the stria terminalis	CNU	Cerebral nuclei	18	3
MD	Mediodorsal nucleus of thalamus	TH	Thalamus	13	-1
LGv	Ventral part of the lateral geniculate complex	TH	Thalamus	10	-1
PVH	Paraventricular hypothalamic nucleus	HY	Hypothalamus	12	15
DMH	Dorsomedial nucleus of the hypothalamus	HY	Hypothalamus	13	15
AHN	Anterior hypothalamic nucleus	HY	Hypothalamus	12	15
SUM	Supramammillary nucleus	HY	Hypothalamus	13	-1
MPN	Medial preoptic nucleus	HY	Hypothalamus	12	15
PVHd	Paraventricular hypothalamic nucleus descending division	HY	Hypothalamus	12	16
VMH	Ventromedial hypothalamic nucleus	HY	Hypothalamus	13	15
MRN	Midbrain reticular nucleus	MB	Midbrain	14	10
NLL	Nucleus of the lateral lemniscus	HB	Hindbrain	30	27
CS	Superior central nucleus raphe	HB	Hindbrain	16	10
NTS	Nucleus of the solitary tract	HB	Hindbrain	0	9
SPVO	Spinal nucleus of the trigeminal oral part	HB	Hindbrain	0	9
LING	Lingula (I)	CB	Cerebellum	0	9
CENT2	Lobule II	CB	Cerebellum	0	9
CENT3	Lobule III	CB	Cerebellum	0	9
CUL4 5	Lobules IV-V	CB	Cerebellum	0	9
DEC	Declive (VI)	CB	Cerebellum	0	9
FOTU	Folium-tuber vermis (VII)	CB	Cerebellum	0	9
PYR	Pyramus (VIII)	CB	Cerebellum	0	9
UVU	Uvula (IX)	CB	Cerebellum	0	9
NOD	Nodulus (X)	CB	Cerebellum	0	9
SIM	Simple lobule	CB	Cerebellum	0	9

Allen acronym	**Allen name**	**Cosmos acronym**	**Cosmos name**	**Inter-trial**	**Audio-visual cue**
ANcr1	Crus 1	CB	Cerebellum	0	12
ANcr2	Crus 2	CB	Cerebellum	0	9
PRM	Paramedian lobule	CB	Cerebellum	0	9
COPY	Copula pyramidis	CB	Cerebellum	0	9
PFL	Paraflocculus	CB	Cerebellum	0	9
FL	Flocculus	CB	Cerebellum	0	9